

N73-21610

FILE  
COPY

RESEARCH IN PLASMA PHYSICS

FINAL TECHNICAL REPORT

Contract No. NASW-2302

February 1973

prepared for

HEADQUARTERS

NATIONAL AERONAUTICS AND SPACE ADMINISTRATION

Washington, D.C.

 AVCO EVERETT RESEARCH LABORATORY, INC.

A SUBSIDIARY OF AVCO CORPORATION

RESEARCH IN PLASMA PHYSICS  
FINAL TECHNICAL REPORT

AVCO EVERETT RESEARCH LABORATORY, INC.  
a subsidiary of Avco Corporation  
Everett, Massachusetts

Contract No. NASW-2302

February 1973

prepared for  
HEADQUARTERS  
NATIONAL AERONAUTICS AND SPACE ADMINISTRATION  
Washington, D. C.

## ABSTRACT

Three aspects of barium ion cloud dynamics are discussed. First, the effect of the ratio of ion cloud conductivity to background ionospheric conductivity on the motion of barium ion clouds is investigated and compared with observations of barium ion clouds. This study has led to the suggestion that the conjugate ionosphere participates in the dynamics of barium ion clouds. Second, analytic work on the deformation of ion clouds is presented and found to be qualitatively different from that found recently by Simon and Sleeper. Third, the linearized stability theory of Linson and Workman has been extended to include the effect of the finite extent of an ion cloud as well as the effect of the ratio of ion cloud to ionospheric conductivities.

The stability properties of a plasma with contra-streaming ion beams parallel to a magnetic field are investigated. The results are interpreted in terms of parameters appropriate for collisionless shock waves. It is found that this particular instability can be operative only if the upstream Alfvén Mach number exceeds 5.5.

## TABLE OF CONTENTS

<u>Section</u>		<u>Page</u>
	Abstract	iii
	List of Illustrations	vii
I.	INTRODUCTION	1
II.	BARIUM CLOUD STUDIES	3
	A. INTRODUCTION	3
	B. MOTION OF BARIUM ION CLOUDS	9
	C. DEFORMATIONS OF ION CLOUDS	19
	D. SCALE SIZE OF STRIATIONS	29
	References	38
III.	ION STREAMING INSTABILITIES WITH APPLICATION TO COLLISIONLESS SHOCK WAVE STRUCTURE	39
	A. INTRODUCTION	39
	B. LINEAR THEORY	45
	C. RELEVANCE FOR SHOCK WAVE STRUCTURE	54
	D. SUMMARY	61
	References	64

## LIST OF ILLUSTRATIONS

<u>Figure</u>		<u>Page</u>
II. 1	Simple Two-Dimensional Model	4
II. 2	Changes in the Ionospheric Current Flow Due to the Presence of a Highly Conducting Barium Ion Cloud	7
II. 3	Effect of Polarization Field Induced by the Ion Cloud	10
II. 4	Coupling Neglecting the Influence of the Conjugate Ionosphere	13
II. 5	Coupling Including the Influence of the Conjugate Ionosphere	15
II. 6	Sketch of Magnetospheric Current Flows which Couple the Conjugate Ionosphere and the Barium Cloud	18
II. 7	Normalized Density Profiles in the Limits of Very Low Density and Very High Density Clouds Compared to a Gaussian Profile	23
II. 8	Equipotentials Resulting from the Solution Given in Equation (II. 10)	25
II. 9	Deformations of Contours Resulting from Power Series Expansion of the Streamlines in Time	26
II. 10	Linear Wave Spectrum	33
II. 11	Redwood Striations Viewed Directly Up the Magnetic Field Line (Technology International Corporation)	35
II. 12	Spruce Striations Viewed Directly Up the Magnetic Field Line (Technology International Corporation)	36
III. 1	Schematic of the Dispersion Relation Showing the Interaction Regions Leading to Beam-Cyclotron (BC) and Beam-Whistler (BW) Instabilities	43
III. 2	Superposition of the Whistler ( $W_+$ ) and Ion Cyclotron ( $IC_+$ ) Modes for $\delta = 0$ with a Weak Beam Mode	49

<u>Figure</u>		<u>Page</u>
III. 3	The Dispersion Relation (III. 8) for: a) $\delta = 0.1$ , $M_d = 3$ ; b) $\delta = 0.1$ , $M_d = 7$ ; c) $\delta = 0.5$ , $M_d = 3$ ; d) $\delta = 0.5$ , $M_d = 7$	52
III. 4	Range of Unstable Values of $k$ as a Function of Relative Drift Velocity for a) $\delta = 0.1$ and b) $\delta = 0.5$	53
III. 5	Sketch of the Ion Velocity Distribution Function Indicating the Assumed Linear Variation Through the Shock	56
III. 6	The Dispersion Relation III. 8 in the Shock Frame for the Four Cases Shown in Fig. III. 3 where $\omega_s = \omega + \mathbf{k} \cdot \mathbf{V}_e$	59
III. 7	Range of Unstable Wavenumbers as a Function of Upstream Alfvén Mach Number at Two Positions within the Front at a) $\zeta = 0.05$ and b) $\zeta = 0.2$	60
III. 8	Range of Alfvén Mach Numbers for Which Unstable Whistlers will Stand in the Shock as a Function of Position within the Shock	62

## I. INTRODUCTION

During the past year significant progress has been achieved in both areas of study under the present contract. The principal results obtained are reviewed in the following two section. The work reported in Section II on the dynamics of barium ion clouds was performed by L. M. Linson while the work reported in Section III on streaming instabilities was performed by K. Golden, L. M. Linson, and A. Sivasubramanian.

As a result of Project Secede sponsored by the Advanced Research Projects Agency during which barium ion clouds formed from different size payloads were released at various altitudes, it was possible to test theoretical ideas concerning the motion of barium ion clouds. This study has led to the suggestion that the conjugate ionosphere participates in the dynamics of barium ion clouds as discussed in Section II. A and presented at the Fall Meeting of the AGU in San Francisco, California, in December 1971. Analytic work on the deformation of ion clouds is discussed in Section II. B where it is shown that a recent treatment by A. Simon of the University of Rochester is incorrect. A note to that effect will be submitted shortly to the J. G. R. for publication. Unique observations of ion cloud striations made during Project Secede II by looking up the magnetic field have led to an extension of the linear theory presented earlier by Linson and Workman. This analysis is given in Section III. C and was presented at the Annual Meeting of the Division of Plasma Physics in Monterey, California, in November 1972.

In Section III we report the results of a study of the stability properties of a plasma with contra-streaming ion beams and interpret these results in terms of parameters appropriate for collisionless shock waves. We find that this particular instability can be operative only if the upstream Alfvén Mach number exceeds 5.5. A paper based on this work is being prepared for submission to the Physics of Fluids.

## II. BARIUM CLOUD STUDIES

### A. INTRODUCTION

We have previously<sup>1</sup> described some of the results that can be obtained from a simple two-dimensional model for barium ion clouds released in the ionosphere. Recently, Zabusky, Perkins, and Doles<sup>2</sup> have given a careful derivation of the coupled nonlinear differential equations that have been useful for describing the dynamics of barium ion clouds. These equations can also be obtained by starting with simplified equations of motion for electrons and ions in the limit of zero electron collision frequency. The resulting two-dimensional equations express the conservation of electron flow and zero divergence of the total current. In a purely two-dimensional model everything is uniform parallel to the magnetic field and there is no flow of either species in the vertical direction. However, the same two-dimensional equations also represent the limit of vanishingly small parallel resistivity in which the electrons are allowed to flow freely up and down the magnetic field lines but ions are restrained to flow perpendicular to the magnetic field in response to the transverse electric fields.

Figure II. 1 shows a schematic of the cross section of the ion cloud in the plane perpendicular to the magnetic field. The ion cloud is moving to the right with respect to the neutrals. In the two-dimensional model, the ratio of height-integrated conductivities;  $\Sigma_p^c / \Sigma_p^a$ , can be represented as the ratio of the cloud center density,  $N_c$ , to the ambient ionospheric

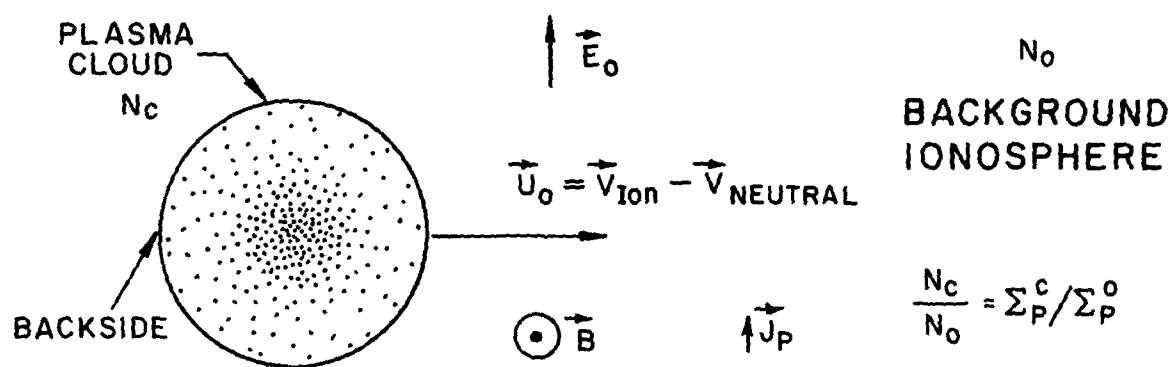


Fig. II. 1 Simple Two-Dimensional Model

density,  $N_0$ . Due to the slow rate of development of the ion cloud and the small plasma pressure relative to the magnetic field pressure (low  $\beta$ ), the ambient electric fields are electrostatic as expressed by the condition  $\nabla \times \vec{E} = 0$ . Since the electrons do not experience any collisions they flow at the local  $\vec{E} \times \vec{B}/B^2$  velocity. The flow of the ionization is thus incompressible due to the assumption of electrostatic fields. The fact that the flow transverse to the magnetic field is incompressible is extremely important in theoretically determining the behavior of barium ion clouds. This assumption precludes the possibility of an electron density increase. The ion motion closely follows the electron motion but the ions do have a component of velocity in the direction of the electric field as a result of collisions with the neutrals. At high altitudes the ion velocity with respect to the neutrals is given approximately by

$$\vec{V}_i = \frac{\vec{E} \times \vec{B}}{B^2} + \frac{1}{\kappa_i} \frac{\vec{E}}{B}. \quad (\text{II. 1})$$

where  $\kappa_i = m_i/eB\tau$  and  $\tau$  is the ion-neutral collision frequency.

The simple set of coupled nonlinear differential equations that describe the motion of barium ion clouds transverse to the magnetic field are:

$$\frac{\partial N}{\partial t} + \frac{\vec{E} \times \vec{B}}{B^2} \cdot \nabla N = 0; \quad (\text{II. 2})$$

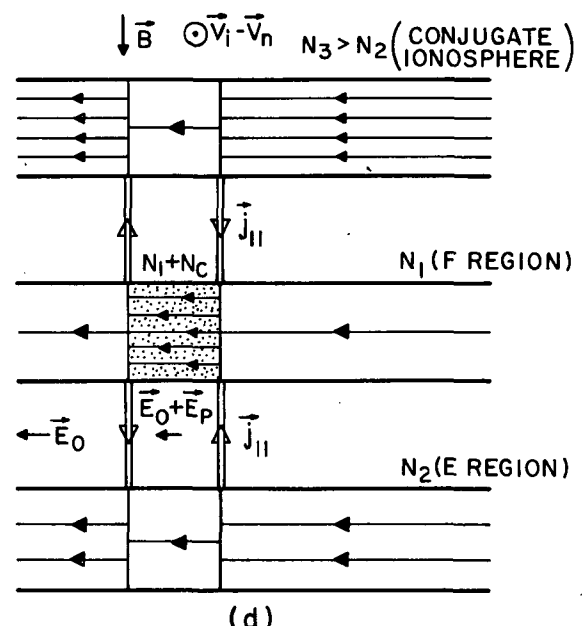
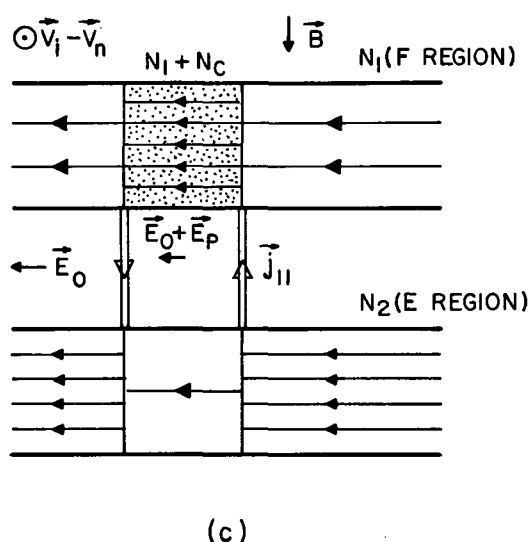
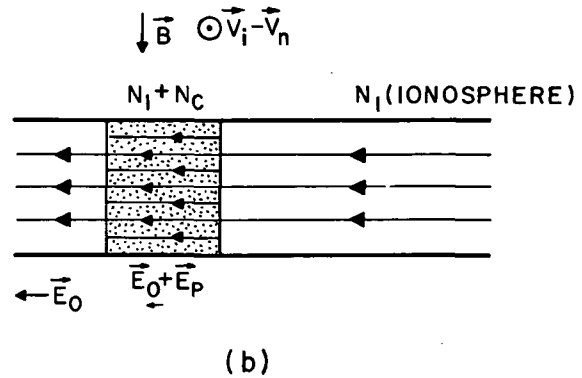
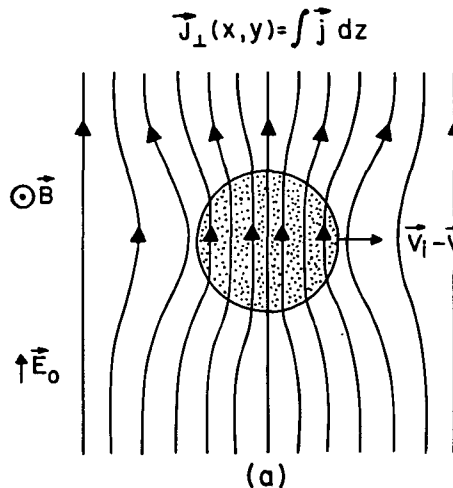
$$\nabla \cdot \vec{J}_p \propto \nabla \cdot N \vec{E} = 0; \quad (\text{II. 3})$$

$$\nabla \times \vec{E} = 0. \quad (\text{II. 4})$$

Equation (II. 2) is the continuity equation for the incompressible flow of the electrons at the local  $\vec{E} \times \vec{B}/B^2$  velocity. Equation (II. 3) describes the conservation of the current flow perpendicular to the magnetic field in the ionosphere and Eq. (II. 4) is the quasistatic assumption of the low- $\beta$  approximation. The Pedersen current,  $\vec{J}_p$ , is proportional to the product of the conductivity, N (proportional to the ion density), and the electric field,  $\vec{E}$ , all measured in the frame of the ambient neutrals.

These equations have been used to investigate the stability of the backside of barium ion clouds<sup>3, 4</sup>, as well as other edges<sup>5</sup>, and the non-linear development of striations<sup>6</sup>. Here we shall discuss how these simple equations have successfully been applied to describe the motion of barium ion clouds<sup>7</sup>, their deformations including the steepening of the backside<sup>6</sup>, and the predominant scale length of striations<sup>8</sup>. First we describe in a simple way the relationship of this two-dimensional model to a more realistic layered ionosphere.

When the barium ion cloud is considered to be of finite extent parallel to  $\vec{B}$ , currents flowing in the ionosphere below the cloud are affected by the presence of the ion cloud and give rise to currents flowing parallel to the magnetic field. In Fig. II. 2 we indicate qualitatively the effect that the presence of the highly conducting barium ion cloud has on the current flow pattern in the ionosphere. Figure II. 2a is a schematic diagram in the plane perpendicular to the magnetic field showing the distortion of the current flow due to the presence of the more conducting ion cloud. In a completely two-dimensional model this same current flow pattern would exist at every altitude parallel to the magnetic field and drift



D3512

(c)

Fig. II. 2 Changes in the Ionospheric Current Flow Due to the Presence of a Highly Conducting Barium Ion Cloud; a) Height-Integrated Current Density Flowing Perpendicular to the Magnetic Field; This Same Pattern Results in the Cases of b) a One-Layered Ionosphere, c) a Two-Layered Ionosphere, and d) Local Plus Conjugate Ionosphere

as a "current cell" with the  $\vec{E} \times \vec{B}/B^2$  velocity. That situation is shown schematically in Fig. II. 2b which represents a cut in the yz plane through the center of the ion cloud. Note that the current density in the ion cloud is larger than in the less dense ionosphere. From Fig. II. 2a we see that this increase results from the concentration of the current in the ion cloud.

In Fig. II. 2c the horizontal currents are the ion Pedersen currents whereas the parallel currents are due to electrons flowing along the magnetic field. Figure II. 2d represents a generalization to a three-layered ionospheric model. The more conducting layer at the top of this figure represents a conjugate ionosphere which may be highly conducting and therefore can contribute a large perpendicular current density. Again the presence of a conducting ion cloud in the local ionosphere can effect the current flow in the conjugate ionosphere since electron currents flow freely along the magnetic field through the magnetosphere.

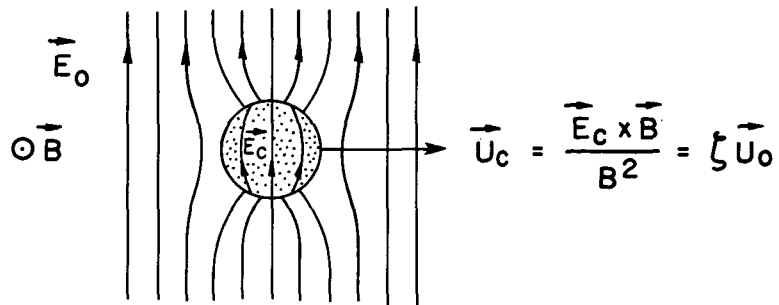
While it is recognized that the diagrams given in Fig. II. 2c and II. 2d are qualitatively correct insofar as they indicate current flow in different layers of the ionosphere, they are strictly correct only if (1) there is no distinction between the barium ions and the ambient ionospheric ions; (2) if the neutral density is the same in all three layers; and (3) if the electric field which drives the currents is externally imposed on the complete system. The actual interaction of several different layers in the ionosphere with a barium ion cloud is only now beginning to be considered and is a very complex problem. It is clear that the plasma density will be increased where the electrons flow into the lower ionosphere and decreased where electrons leave to neutralize the charge accumulation in the cloud. Thus

the ionosphere subtended by the cloud will be locally perturbed and this perturbation will move with the cloud.

We can see qualitatively that the effect of an ion cloud on the current flow pattern depends sensitively on the cloud conductivity compared to the conductivity of the ionosphere. The appropriate parameter that characterizes the cloud-ionosphere interaction is the ratio of the height-integrated Pedersen conductivity of the barium ion cloud to the height-integrated Pedersen conductivity of the ambient ionosphere.

## B. MOTION OF BARIUM ION CLOUDS

Equation (II. 3) indicates that at any instant in time the electric field depends on the distribution of ionization in the ion cloud. In particular the polarization electric field due to the presence of the ion cloud reduces the total field at the center of the cloud as indicated at the top of Fig. II. 3. As a result, the center of the ion cloud moves with a slower velocity with respect to the neutrals than does a background ion that is flowing with the velocity  $\vec{U}_o$ . The value of the electric field at the center of the ion cloud depends on the ratio of the height -integrated Pedersen conductivity of the ion cloud,  $\Sigma_p^c$ , to the height-integrated Pedersen conductivity of the background ionosphere,  $\Sigma_p^a$ , as well as on the distribution of ionization in the ion cloud. For a uniform ionosphere and a constant neutral density,  $\Sigma_p^c/\Sigma_p^a$  can also be expressed as the ratio of height-integrated cloud density to ambient density,  $N_c/N_o$ . The electric field at the center of the ion cloud, and thus its motion, can be expressed in terms of a coupling parameter,  $\zeta$ , defined as the ratio of the electric field at the center of the ion cloud (in the frame of the ambient neutrals) to the external electric field,



$$\nabla \cdot \vec{N} \vec{E} = 0 ; \quad \vec{E} = \vec{E}_0 + \vec{E}_p \implies \nabla \cdot \vec{E}_p = -\vec{E} \cdot \nabla \ln [1 + N_c(r)/N_0]$$



$$U_c = \frac{E_0 / B}{1 + \frac{a}{a+b} \frac{N_c}{N_0}}$$

$a \gg b$

$a = b$

$$U_c = \frac{E_0 / B}{1 + \frac{N_c}{N_0}}$$

$$U_c = \frac{E_0 / B}{1 + \frac{1}{2} \frac{N_c}{N_0}}$$

$$U_c = \zeta E_0 / B$$

$$\zeta \sim \begin{cases} 1 - \frac{1}{2} \frac{N_c}{N_0} ; & N_c \ll N_0 \\ \sqrt{3} (N_c / N_0)^{-3/4} ; & N_c \gg N_0 \end{cases}$$

C8769

Fig. II. 3 Effect of Polarization Field Induced by the Ion Cloud

$$\vec{E}_c = \vec{E}_o + \vec{E}_{pc} = \zeta \vec{E}_o, \quad (\text{II. 5})$$

where the subscript  $c$  represents the value at the center of the ion cloud.

Since the difference in velocity between the ion cloud and the neutral wind is frame independent and equal to  $\vec{E}_c \times \vec{B}/B^2$ , Eq. (II. 5) implies

$$\vec{V}_i - \vec{V}_n = \vec{U}_c = \zeta \left( \frac{\vec{E}_a \times \vec{B}}{B^2} - \vec{V}_n \right) = \zeta \vec{U}_o. \quad (\text{II. 6})$$

This equation also defines the frame invariant velocity of the ion cloud,  $\vec{U}_c$ . It follows that  $\zeta$  ranges between one and zero for very small and very large ion clouds respectively;

$$\zeta \rightarrow 1, \quad \vec{V}_i \rightarrow \frac{\vec{E}_a \times \vec{B}}{B^2}, \quad (N_c \ll N_o);$$

$$\zeta \rightarrow 0, \quad \vec{V}_i \rightarrow \vec{V}_n, \quad (N_c \gg N_o). \quad (\text{II. 7})$$

Very small clouds or low density perturbations provide a direct measure of the ambient electric field,  $\vec{E}_a = -\vec{V}_i \times \vec{B}$ , while very large clouds are completely tied to the neutral wind.

Theoretical models have been explored that give analytic expressions for the dependence of  $\zeta$  on  $N_c/N_o$ . An example will be given in the next section. A well-known example corresponds to a cloud of constant density  $N_c$  with an ellipsoidal cross section as illustrated in Fig. II. 3. Two interesting limits, a circular cloud with  $a = b$  and an elongated cloud with  $b \ll a$  are also shown. The former is the shape used by Haerendel, Lüst,

and Reiger<sup>9</sup> in deriving their now classic equation for determining the ambient electric field from the motion of barium ion clouds. In the high altitude limit ( $\kappa_i \gg 1$ ), their equation can be brought into the form of Eq. (II. 6) if the identification  $\zeta = 2/(1 + \lambda^*)$  is made where  $\lambda^* = (N_o + N_c)/N_o$ . The elongated shape is most tied to the neutral wind and its motion corresponds to that of a field-aligned sheet of ionization. The degree of coupling also depends on the density profile of the ionization for large density clouds. A cylindrically symmetric cloud with a density profile  $N \propto (1 + r^2)^{-4/3}$  is less coupled to the neutral wind for the same value of peak column concentration as indicated on the right-hand side of Fig. II. 3 and discussed in the next section.

Figure II. 4 is a plot of the coupling parameter as a function of the ratio of cloud conductivity to ionospheric conductivity for several barium releases sponsored by ARPA in Project Secede. The estimated uncertainties in the values for  $\zeta$  are indicated by the vertical error bars, the horizontal error bars indicate a factor of two uncertainty in the estimates for the ratio of integrated conductivities. The two curves illustrate the two extremes in coupling that depend on the configuration of the ionization. The sheet-like shape is strongly coupled to the neutral wind, whereas the least coupled is the cylindrically symmetric cloud with a monotonic, radial density profile. A first glance at the data would suggest that the simple theory is inadequate to describe the degree of coupling of ion clouds to the neutral wind. We see that only the daytime and summer morning releases come near to agreeing with the theory. Note the large disagreement for the winter evening releases since the scale on the bottom is logarithmic and covers several decades.

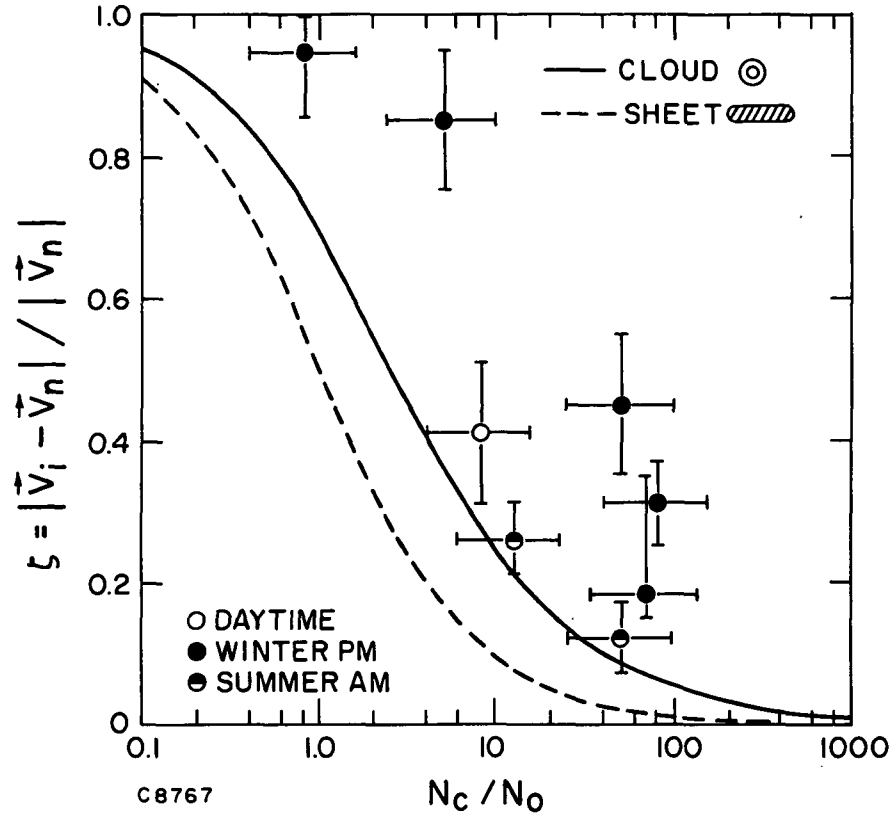


Fig. II. 4 Coupling Neglecting the Influence of the Conjugate Ionosphere. The open circle is event Quince while the half-filled circles are events Apple and Dogwood. In order from largest coupling parameter to smallest, the solid dots are the Plum Puff, Redwood, Plum, Spruce, and Nutmeg clouds respectively.

Thus the ion clouds are observed to separate from the corresponding neutral clouds much faster than the simple theory would allow. They behave as though the background ionosphere were far more conducting than the measurements of the ambient ionosphere indicate.

The observation that the winter evening releases are those that are in most serious disagreement with the theory led to the suggestion that the conjugate ionosphere in the southern hemisphere was contributing to the background ionospheric conductivity. This suggestion seemed plausible because the ionosphere conjugate to Eglin (at  $54^{\circ}$ S,  $103^{\circ}$ W) is further west and was experiencing summer and hence was sunlit. On the other hand, the ionosphere conjugate to the summer morning releases (at  $49^{\circ}$ S,  $66^{\circ}$ W) was experiencing winter and thus was still in darkness. More quantitatively, when the sun was  $9^{\circ}$  below the horizon after sunset at Eglin in the last half of January, 1971, and  $9^{\circ}$  below the horizon before sunrise at Puerto Rico in the first half of May, 1969, the sun was  $26^{\circ}$  above the horizon and  $23^{\circ}$  below the horizon, respectively, at the corresponding conjugate ionospheres. Hence it is reasonable to assume that the height-integrated Pedersen conductivity of the conjugate ionosphere for the winter evening releases had a typical daytime value of 5.0 mho. By adding these conductivities to the local values, we obtain new estimates for the ratio of cloud to ionospheric conductivity.

Figure II.5 is a replotting of the data assuming that the conjugate ionosphere does contribute to the background ionospheric conductivity. By making this assumption we see that there is no longer any disagreement between the simple theory and the data. It is clear that these clouds do

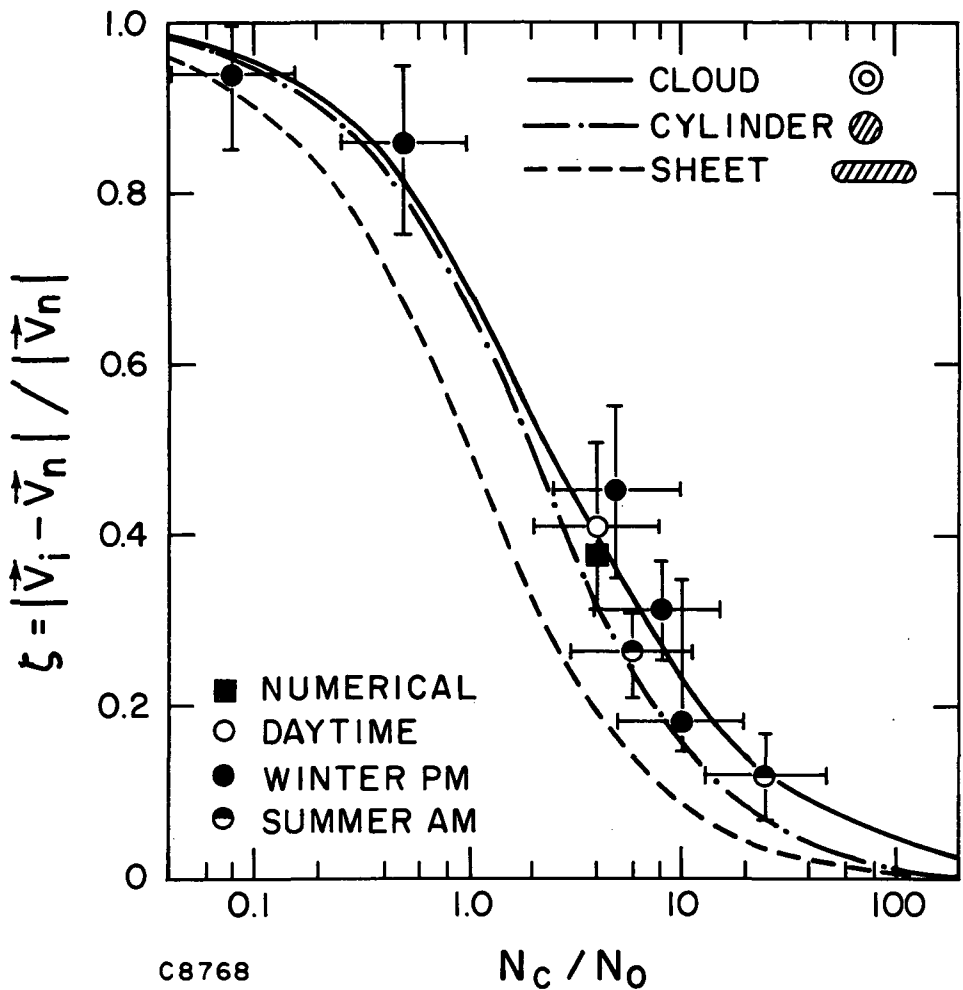


Fig. II. 5

Coupling Including the Influence of the Conjugate Ionosphere. The dots represent the same clouds shown in the preceding figure. The solid square represents the point obtained from numerical modeling.

not move as though they were shaped like sheets. However, the data do not clearly distinguish between the two other cylindrical models whose theoretical curves are shown. Zabusky, Perkins, and Doles<sup>10</sup> have solved Eqs. (II. 2) through (II. 4) by finite difference techniques for a cloud with a cylindrically symmetric initial density distribution,  $N = N_o [1 + 4(1 - r^2/4)^4]$  for  $r < 2$ . The velocity of the peak density in the  $\vec{E} \times \vec{B}$  frame is  $0.63 \vec{V}_n$ . The corresponding value for the coupling parameter,  $\zeta$ , is 0.37. This value for  $N_c/N_o = 4$  is shown as a solid square in Fig. II. 5. We note that this point is in excellent agreement with the analytical models, lying closer to the curve with a density profile (which should provide an upper limit) than to the curve for a cylinder with constant density.

We note that the agreement with the theoretical model includes data in which the ratio of conductivities ranges over two and one-half orders of magnitude. This agreement is highly suggestive that the conjugate ionosphere must participate in the dynamics of the motion of barium ion clouds. We estimate that an Alfvén wave (the propagation velocity of an electromagnetic disturbance) can travel from the northern to the southern hemisphere and back in half a minute, so there is sufficient time to communicate the polarization electric fields between the two hemispheres. The most sensitive test of the theory would be to make a 12 kg size release at dawn and dusk. The degree of coupling with the neutral wind should change from about 65% ( $\zeta = 0.35$ ) to about 30% ( $\zeta = 0.7$ ) for the assumed change of a factor of five in the ratio of conductivities.

There are two other possible explanations for the lack of agreement between data and theory shown in Fig. II. 4; either the data are plotted

incorrectly, or the theoretical treatment is wrong. The largest uncertainty in the velocities listed is the ambient ionospheric velocity,  $\vec{E}_a \times \vec{B}/B^2$ , which has been assumed to be less than 20 m/s where better estimates were not available. The remaining possibility is that the theory does not correctly describe the coupling of the barium cloud to the rest of the ionosphere. It is true that the complications of this interaction are hidden by ascribing to the ionosphere a height-integrated conductivity, a procedure that would be strictly valid only if the value of  $\kappa_i$  outside the cloud were constant and the same as for barium. There is no assessment yet as to the effect to be expected from a more rigorous treatment of the dynamics of the rest of the ionosphere. On the other hand, the assumption that the reconciliation between data and theory is achieved by including the effect of the conjugate ionosphere is a simple and plausible one.

There are several important implications that follow from assuming that the conjugate ionosphere plays a role in the ion cloud dynamics. First is that the cloud-produced polarization electric fields must project into the southern hemisphere which suggests that the assumption that the earth's magnetic field lines are equipotentials for a large distance is reasonable. A second conclusion is that there must be magnetic-field-aligned currents in the magnetosphere, and a third conclusion is that the presence of the ion cloud and its resulting motion in the northern hemisphere must cause a disturbance in the ion density in the conjugate ionosphere in the southern hemisphere. An independent verification of any of these effects would be very valuable.

Let us adopt a simplified model of an ion cloud in the ionospheric-magnetospheric system as shown in Fig. II. 6 in order to make a quantitative

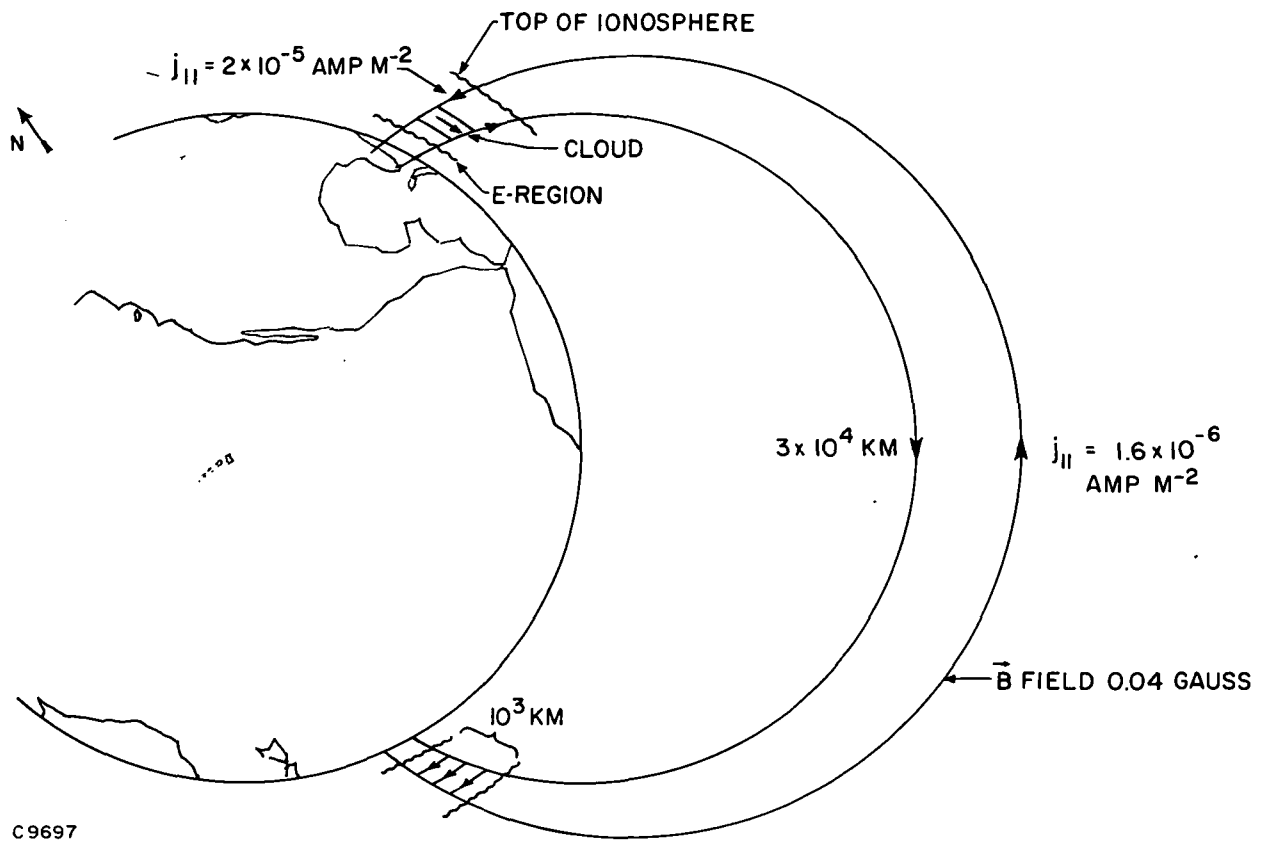


Fig. II. 6 Sketch of Magnetospheric Current Flows which Couple the Conjugate Ionosphere and the Barium Cloud

estimate of some of these effects. We find that the magnetic field lines are highly conducting so that the electric fields do not suffer any appreciable resistive losses in being projected into the conjugate ionosphere. The most important effect is the disturbance in electron density that the current flow in the background ionosphere is likely to make. The parallel currents must be closed by Pedersen currents which are due to the flow of the background ions. This ion flow will lead to significant changes in the local ionospheric density. These changes should be observable by ionosondes. In particular, for the winter evening releases, the motion of the ion clouds should have produced large changes in electron density in the conjugate ionosphere in the southern hemisphere. These changes should have been detectable had ionosondes been deployed there.

### C. DEFORMATIONS OF ION CLOUDS

The electric field varies over the distribution of density in the ion cloud as discussed above and as shown schematically in Fig. II. 3. Since the ionization moves with the local  $\vec{E} \times \vec{B}/B^2$  velocity, different parts of the ion cloud move with different velocities. Thus, as the ion cloud moves, its shape distorts. Here we shall present the results of an analytic investigation of the changes in shape of equal density contours obtained by expanding the solution of the nonlinear equations for the equipotentials (streamlines) as a power series in time. We shall see that there are qualitative differences between the contours obtained here and those recently presented by Simon and Sleeper.<sup>17</sup> We shall point out that they obtained incorrect deformations because they did not carry through their expansion procedure correctly.

We write the electric field as the sum of the externally imposed uniform field,  $\vec{E}_o$ , plus the polarization field,  $\vec{E}_p$ , due to the presence of the

ion cloud;

$$\vec{E} = \vec{E}_o + \vec{E}_p = \vec{E}_o - \nabla \phi_p \quad (\text{II. 8})$$

Equation (II. 3) is conveniently rewritten

$$\nabla^2 \phi_p = (\vec{E}_o - \nabla \phi_p) \cdot \nabla L \quad (\text{II. 9})$$

where

$$L = \ln N/N_o = \ln \left( 1 + \frac{\Delta N}{N_o} \right).$$

$\Delta N$  is the additional density due to the presence of the ion cloud.

Equation (II. 9) determines the spatial variation of the polarization field as a function of the ion cloud density distribution. Once  $\phi_p$  is known, Eq. (II. 2) can be used to obtain the changes in density that result. The new density distribution including these changes then produces a new polarization field distribution. It is this last step that was omitted by Simon and Sleeper<sup>11</sup> resulting in their erroneous deformation contours.

We have found a useful self-consistent solution of Eq. (II. 9):

$$\phi_{po} = \rho E_o \frac{\frac{b^2 r \cos \theta}{b^2 + r^2}}{} \quad (\text{II. 10})$$

$$\begin{aligned} L_o(z) = \ln \left( 1 + \frac{\Delta N}{N_o} \right) &= \ln \frac{(1+z)^2}{z^2 + (2+\rho)z + (1-\rho)} \\ &+ \frac{\rho}{\sqrt{8\rho + \rho^2}} \ln \frac{2z + 2 + \rho + \sqrt{8\rho + \rho^2}}{2z + 2 + \rho - \sqrt{8\rho + \rho^2}} \end{aligned} \quad (\text{II. 11})$$

where  $z = (r/b)^2$ . According to this solution, the polarization electric field

at the center of the cloud is

$$\vec{E}_c = -\rho \vec{E}_o. \quad (\text{II. 12})$$

Hence, the parameter  $\rho$  represents the amount of reduction of the background field at the center of the cloud due to the cloud's presence and is equal to  $1 - \zeta$  where  $\zeta$  was defined in the previous section. This decrease in the electric field at the cloud's center makes it easy to see that the region of maximum density does not keep up with the background ionization and thus falls back toward the neutral cloud causing the backside to steepen.

From Eq. (II. 11), we can determine the cloud center density as a function of the parameter  $\rho$  by setting  $z = 0$ :

$$L_o(0) = \ln \left( 1 + \frac{N_c}{N_o} \right) = \ln \frac{1}{1 - \rho} + \frac{\rho}{\sqrt{8\rho + \rho^2}} \ln \frac{(2 + \rho + \sqrt{8\rho + \rho^2})^2}{4(1 - \rho)}. \quad (\text{II. 13})$$

By expanding this equation in the limits  $\rho \ll 1$  and  $\rho \rightarrow 1$ , we obtain the relation between  $\rho$  and the cloud-center density for low- and high-density clouds;

$$\rho \sim \begin{cases} N_c / 2N_o & ; \quad N_c \ll N_o \\ 1 - \frac{\sqrt{3}}{(N_c/N_o)^{3/4}} & ; \quad N_c \gg N_o \end{cases} \quad (\text{II. 14})$$

The half-width,  $a$ , at half-max of the cloud is determined by the equation

$$L_o(a) = \ln \left( 1 + \frac{N_c}{2N_o} \right). \quad (\text{II. 15})$$

In the limit of small  $\rho$  (low cloud density), Eq. (II. 11) can be expanded to yield

$$\frac{\Delta N}{N_o} \sim \frac{2\rho}{(b^2 + r^2)^2}; \quad (N_c \ll N_o) \quad (\text{II. 16})$$

for which the half-width,  $a$ , is given as

$$a = (\sqrt{2} - 1)^{1/2} b = 0.644b. \quad (\text{II. 17})$$

In the opposite limit of large cloud density, we may obtain

$$\frac{\Delta N}{N_o} \sim \frac{3^{2/3}}{(1 - \rho + 3r^2)^{4/3}}; \quad (N_c \gg N_o) \quad (\text{II. 18})$$

for which the half-width,  $a$ , is determined as

$$a \sim \left[ (2^{3/4} - 1) \frac{1 - \rho}{3} \right]^{1/2} b \sim \frac{0.626}{\left( \frac{N_c}{N_o} \right)^{3/8}} b. \quad (\text{II. 19})$$

The normalized cloud density profiles  $\Delta N(r)/N_c$ , as determined by Eq. (II. 11) for the two limiting values of the parameter  $N_c/N_o$  and normalized by their half-width,  $a$ , are shown in Fig. IL 7. A normalized gaussian profile is also shown for comparison. It is seen that the shape of the cloud is fairly reasonable, falling off at large distances as  $r^{-4}$  and  $r^{-8/3}$  for the two cases shown.

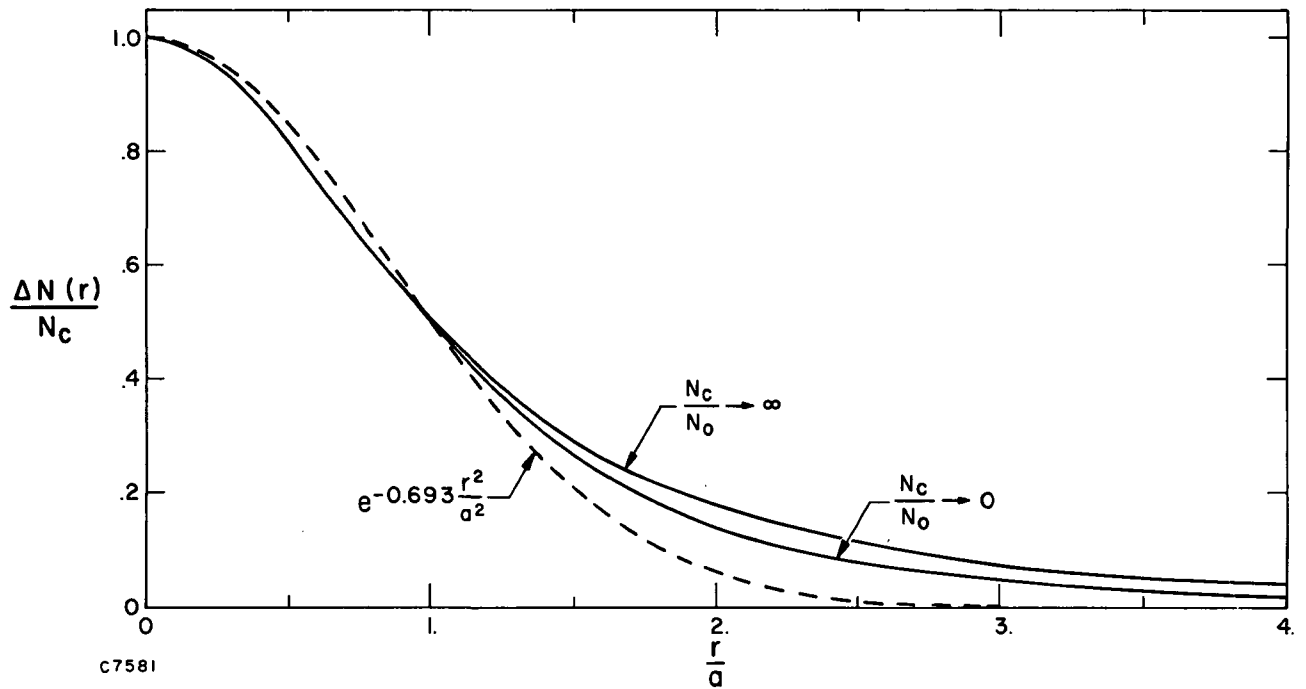


Fig. II. 7 Normalized Density Profiles in the Limits of Very Low Density and Very High Density Clouds Compared to a Gaussian Profile

In the frame moving with the velocity of the background ionosphere,  $\vec{U}_o = \vec{E}_o \times \vec{B}/B^2$ , the equation that describes the deformations of the density contours can be written

$$\frac{\partial N}{\partial t} = \frac{\nabla \phi_p \times \vec{B}}{B^2} \cdot \nabla N \quad (\text{II. 20})$$

From this equation it is easy to see that the equipotentials determined by  $\phi_p = \text{constant}$  are streamlines of the flow. An example of the streamlines derived from Eq. (II. 10) are shown in Fig. II. 8. From Eq. (II. 20) we may calculate the form that the initial displacements within the cloud take. Since the cloud is initially cylindrically symmetric, we need only consider the radial components of the displacements of the contours. We thus have for a small, initial time step

$$\Delta r = v_r \Delta t = \frac{1}{rB} - \frac{\partial \phi_p}{\partial \theta} \Delta t = g(r) \sin \theta \Delta t \quad (\text{II. 21})$$

where  $g$  is a function of radius alone. Hence each equal density contour, originally a set of concentric circles as shown in Fig. II. 8, is displaced initially to the left. There is no change in shape of each density contour.

If the streamlines shown in Fig. II. 8 were constant in time, then the changes in shape of the equal density contour could be easily determined by following the streamlines shown. The deformations that would result are shown in Fig. II. 9a. In actuality, the streamlines are not constant in time but are governed by the time-dependent Eqs. (II. 9) and (II. 20). The changes in density resulting from the displacements given by Eq. (II. 21) produces a

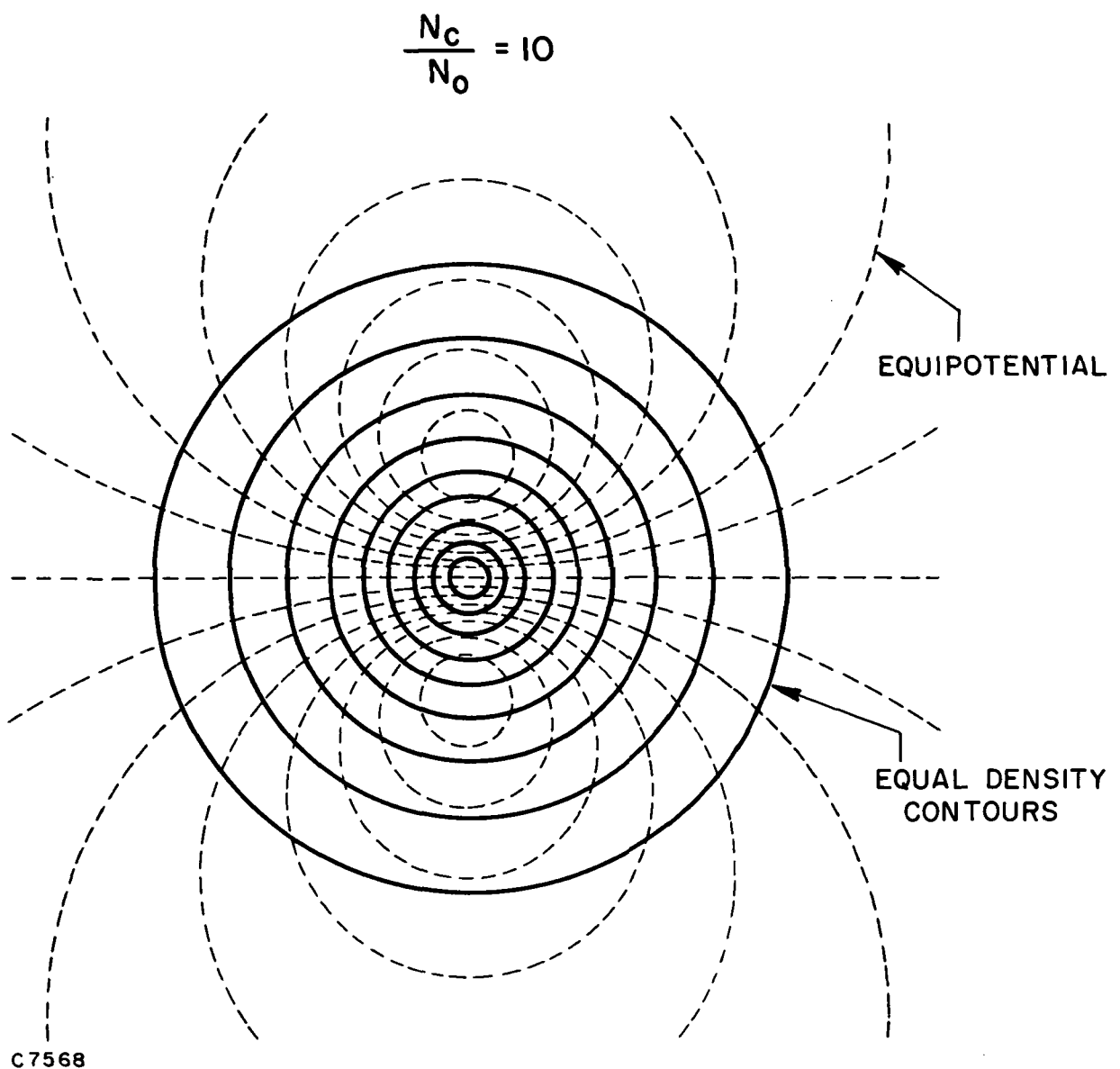


Fig. II. 8      Equipotentials Resulting From the Solution Given in  
Equation (II. 10)

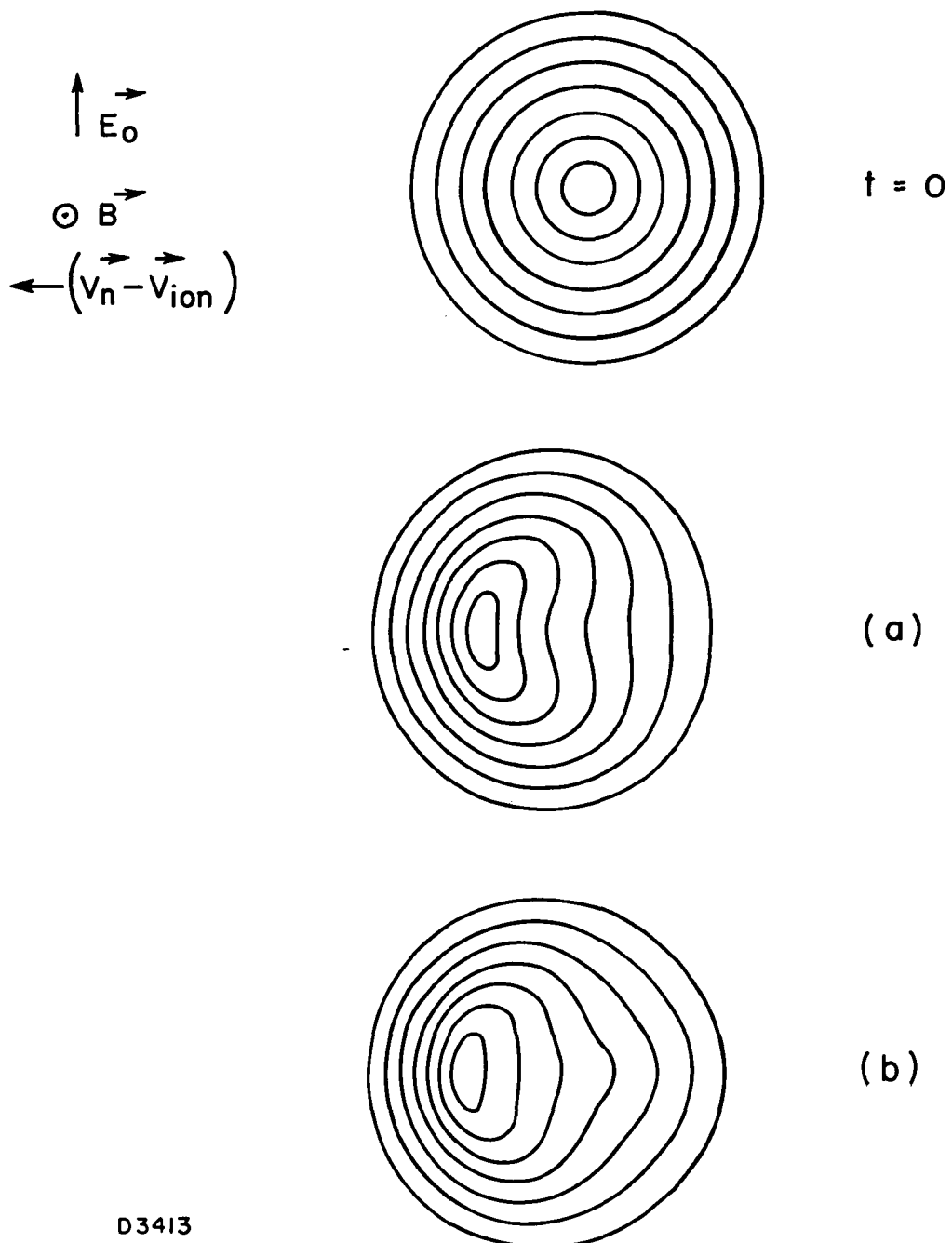


Fig. II. 9 Deformations of Contours Resulting from Power Series Expansion of the Streamlines in Time; a) Zeroth Order Term; b) Zeroth Order Plus First Order Term

new contribution to  $\phi_p$  that changes the streamlines. We shall calculate these changes to next order in time in the form

$$\phi_p(r, \theta, t) = \phi_{po}(r, \theta) \left[ 1 + \rho t f_1(r, \theta) \right] \quad (\text{II. 22})$$

$$L(r, \theta, t) = L_o(r) + \rho t L_1(r, \theta, \rho) \quad (\text{II. 23})$$

where  $\phi_{po}$  and  $L_o$  are given by Eqs. (II. 11) and (II. 10), respectively.  $L_1$  is determined by Eq. (II. 20) and the functions  $\phi_{po}$  and  $L_o$ .  $L_1$  can then be used in Eq. (II. 9) to determine  $f_1$ . It is not possible to solve the resulting equation for  $f_1$  exactly for arbitrary  $\rho$ . The resulting equation is expanded in a power series in  $\rho$  and the first terms of that series have been determined. The resulting expressions are:

$$L_1(r, \theta, \rho) = \frac{b^3}{b^2 + r^2} \frac{\partial L_o(r, \rho)}{\partial r} \sin \theta; \quad (\text{II. 24})$$

$$f_1 = -\frac{2}{3} \frac{r}{b} \sin \theta \left[ 1 + \frac{\rho}{6} \frac{3+z}{(1+z)^2} - \frac{4}{15} \frac{\rho}{(1+z)^4} + O(\rho^2) \right] \quad (\text{II. 25})$$

where  $z = (r/b)^2$ . It is found that the term in  $f_1$  which depends on  $\rho$  makes negligible difference in the resulting deformations of density contours even for the value  $\rho = 1$ . Hence, the neglect of this term altogether is probably reasonable except for the very highest density clouds.

We now have a solution for the time dependent stream functions. The resulting deformations in the density contours when they are allowed to follow these time dependent stream functions are shown in Fig. II. 9b. Note that the higher order term,  $f_1$ , makes a qualitative difference from the changes

in shape shown in Fig. II. 9a. Note that the contours are convex outward on the righthand or front side of the barium ion cloud when the more accurate expression is used. We also note that the backside has become steeper during the same time interval.

The deformations in Fig. II. 9b show several interesting features for which we now have an analytic handle. The first is the steepening of the backside which results from the polarization electric field,  $\vec{E}_p$ , due to the density gradients (or, alternatively, to the increased drag at the center of the ion cloud which pulls the center in the direction of the neutral cloud). The second is the increase in width in the direction transverse to its motion as shown by the high-density contours near the center of the cloud. Since the flow described by Eq. (II. 20) is incompressible, the area within each equal density contour is constant. This increase in width observationally would appear as though the cloud were diffusing and thus this model which assumes no diffusion provides an explanation for the anomalously large "diffusion coefficient" which has been reported for diffusion of ion clouds perpendicular to  $\vec{B}$ . We can also see that there is an elongation of the lower density contours in the direction of cloud motion. In particular, at times longer than that for which Eq. (II. 22) is valid, a long thin neck forms where the center of the cloud had been. Lastly, the deformations shown provide an explanation of the fact that the trailing edge of ion clouds develop a large density gradient when seen from a variety of views.

We shall not discuss the solution for the diffusion and motion of barium ion clouds derived earlier by Simon.<sup>12</sup> Both results differ from the model presented here and are valid only for the case  $N_c \ll N_o$ . We

restrict our attention to the high altitude situation ( $\kappa_i >> 1$ ) where these qualitative differences are quantitatively small. We note that in this limit of negligible diffusion Simon and Sleeper's<sup>11</sup> Eqs. (8) and (16) are equivalent to our Eqs. (II. 2) and (II. 3) for the dynamics of barium ion clouds. However, they have neglected the contributions to the deformations resulting from the changes in density. Thus their deformed contours (see their Fig. 1) correspond to the incorrect one shown in Fig. II. 9a. The reason for their error is probably related to the fact that they attempted to present a solution correct to first order in  $\rho$ . The term that gives rise to the differences is the second term of Eq. (II. 22) which is of second order in  $\rho$  for any finite time. However, for times that are appreciable fractions of  $Ba/\rho E_0$ , this term gives rise to the qualitative differences shown.

The deformations given by Fig. II. 9b agree qualitatively with observations of barium ion clouds while those represented by Fig. II. 9a and given by Simon and Sleeper do not. The most striking feature is the steepening of the backside (the bunching of the density contours on the left hand side). The broadening of the highest density contours transverse to the direction of motion is also evident as well as the tendency for the lower density contours to elongate in the direction of motion. Zabusky, Perkins, and Doles<sup>10</sup> have numerically integrated Eqs. (II. 2) and (II. 3) for the case of an initially cylindrically symmetric ion cloud with  $N_c/N_o = 4$ . Their results agree qualitatively with that shown in Fig. II. 9b.

#### D. SCALE SIZE OF STRIATIONS

The major criticism of Linson and Workman's<sup>3</sup> early work is that it represents the stability of an infinite half-plane with infinite density far

to the right and zero density far to the left. That analysis has recently been extended in several ways, primarily by taking into account the finite extent of the back edge of an ion cloud as well as the finite ratio of ion cloud conductivity to the background conductivity.

The basic equations used in the stability analysis are Eqs. (II. 2) and (II. 3) with two modifications. The first is that if we include electron collisions, we obtain a term  $\nabla \cdot D_{\perp} \nabla N$  on the right-hand side of Eq. (II. 2). Here  $D_{\perp} = K(T_e + T_i)m_e v_e^2 e^2 B^2$  is the ambipolar electron-collision-controlled diffusion coefficient. The electron collision frequency,  $v_e$ , is taken to be a constant even though for high density clouds collisions with ions dominate collisions with neutrals. The second modification is related to the fact that we will be analyzing a one-dimensional slab model as an approximation to a local analysis on the back edge of an ion cloud. Hence the unperturbed electric field that should appear in Eq. (II. 2) is the electric field  $\vec{E}_c = \zeta \vec{E}_o$  that exists at the edge of the ion cloud due to its polarization. Alternatively, the unperturbed velocity  $\vec{E} \times \vec{B}/B^2$  should be the velocity of the back edge of the ion cloud,  $\vec{U}_c$ , with respect to the neutrals given by Eq. (II. 6). For large clouds, this velocity is considerably different from the ambient flow velocity  $\vec{U}_o = \vec{E}_o \times \vec{B}/B^2$  (see Fig. II. 5).

The zeroth order density profile whose stability is analyzed is

$$N = \begin{cases} N_o & x < 0 \\ N_o e^{x/d} & 0 < x < x_o \\ N_o + N_c & x_o < x \end{cases} = d \ln(1 + N_c/N_o) \quad (\text{II. 26})$$

Note that the logarithmic density gradient length  $d = x_o / \ln(1 + a)$  is given by the extent of the back edge,  $x_o$ , and the ratio of cloud to ionospheric conductivities,  $a = N_c / N_o$ . A straight-forward linearization of Eqs. (II. 2) and (II. 3) results in the following equation for the  $x$ -variation of the perturbed potential,

$$N \phi'' + \phi' N' - k^2 \left( N - \frac{U_c N'}{\gamma_o} \right) \phi = 0 \quad (\text{II. 27})$$

where the growth rate  $\gamma$  is given by

$$\gamma = \gamma_o - k^2 D_{\perp}. \quad (\text{II. 28})$$

The  $y$ -variation of the perturbations has been taken to be  $\exp(i k y)$ . The problem is solved when the boundary conditions of vanishing potential at  $x \rightarrow \pm \infty$  determine unique values of  $\gamma_o$ .

Equation (II. 27) can be solved piecewise for the unperturbed density distribution given by Eq. (II. 26). By applying the continuity of  $\phi$  and  $\phi'$  at  $x = 0$  and  $x = x_o$ , and defining

$$K = \left[ k^2 \left( 1 - \frac{U_c}{\gamma_o d} \right) + \frac{1}{4d^2} \right]^{1/2}, \quad (\text{II. 29})$$

the equation that determines  $\gamma_o$  implicitly can be put in the form

$$\tan K x_o = \frac{2K}{\left( \frac{U_c}{\gamma_o d} - 1 \right) k}. \quad (\text{II. 30})$$

Some useful limiting solutions of this equation are:

$$\gamma = \begin{cases} k U_c \tanh \frac{a}{2} - k^2 D_{\perp}; & kd \ll 1 \\ \frac{U_c}{d} \left[ 1 - \frac{1 + \pi^2/a^2}{4(kd)^2} \right] - k^2 D_{\perp} & kd \gg 1 \\ \frac{a k U_c}{2 + a k d} - k^2 D_{\perp}; & a \ll 1 \quad (d \text{ fixed}) \\ \frac{k U_c}{(1 + 4k^2 d^2)^{1/2}} - k^2 D_{\perp}; & a \gg 1 \end{cases} \quad (\text{II. 31})$$

From these forms we see that long wavelengths are stabilized by the finite size of the cloud while short wavelengths are stabilized by diffusion. There is a wavelength for maximum growth that can easily be derived from the approximate expression

$$\gamma \sim \frac{U_c}{d} \left[ 1 - \frac{1}{4(kd)^2} \right] - k^2 D_{\perp} \quad (\text{II. 32})$$

yielding

$$\lambda_{\text{peak}} = 2\pi d \left( \frac{4D_{\perp}}{U_c d} \right)^{1/4}. \quad (\text{II. 33})$$

A typical linear-wave spectrum is shown in Fig. II. 10. There is a wavelength for maximum growth, but it should be pointed out that the wavenumber scale is logarithmic and there is a significant growth rate for a wide range of different scale sizes. It is reasonable to expect a variety of wavelengths attempting to grow initially. It should be emphasized that

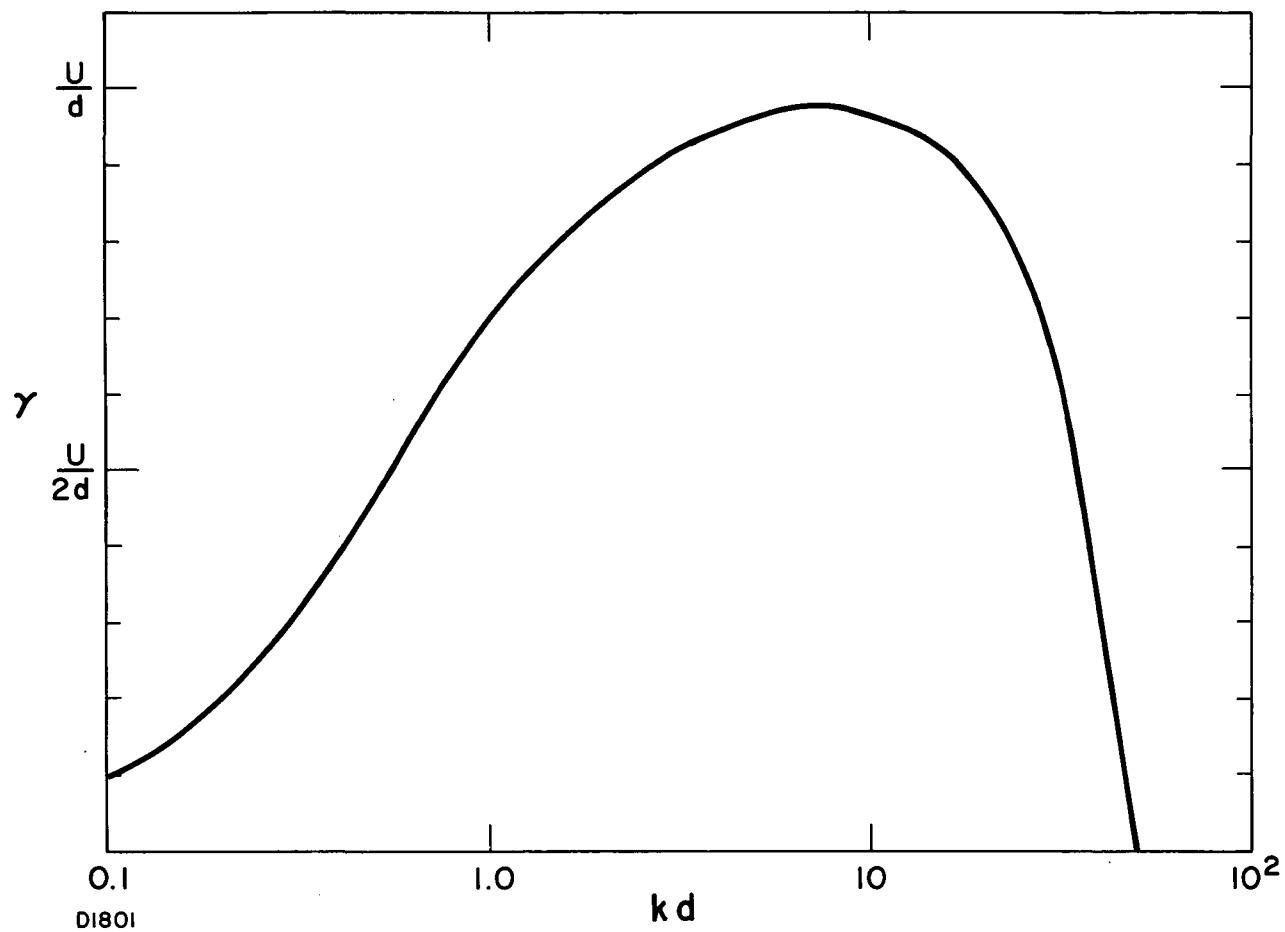


Fig. II. 10 Linear Wave Spectrum

the value of the wavelength for maximum growth depends sensitively on the parameter  $d = |\nabla \ln N|^{-1}$  which so far can only be estimated for large density barium ion clouds that have steepened.

We will now compare the results of the above analysis with observations of barium ion clouds made at Eglin AFB in January 1971. The unique aspect of these releases is that three clouds, Nutmeg, Spruce, and Redwood, released at altitudes of 150 km, 185 km, and 255 km respectively, passed through the magnetic zenith at a time when they were striated. Figs. II. 11 and II. 12 are photographs of Redwood and Spruce, respectively. We note that there is a good deal of structure evident as the striations are highly nonlinear. However, there is an overall sheet-like structure evident in both photographs. The width of the sheets are compared to the results of the linear theory in Table II. 1.

TABLE II. 1 Dominant Scale Size of Striations

	REDWOOD 255 km	SPRUCE 185 km	NUTMEG 150 km
OBSERVED	300-500 m	400 m	250 m
THEORY $\left\{ \begin{array}{l} d = 500 \text{ m} \\ d \propto a \end{array} \right.$	170 m	400 m	500 m
	340 m	400 m	300 m

The appropriate values for  $U_c$  and  $D_{\perp}$  were used for each ion cloud. We see that the uniform assumption that  $d = 500 \text{ m}$  does not give good agreement with the observed dominant wavelength. However, if  $d = 500 \text{ m}$  is assumed appropriate for Spruce and  $d$  is scaled to the initial transverse width,  $a$ , of

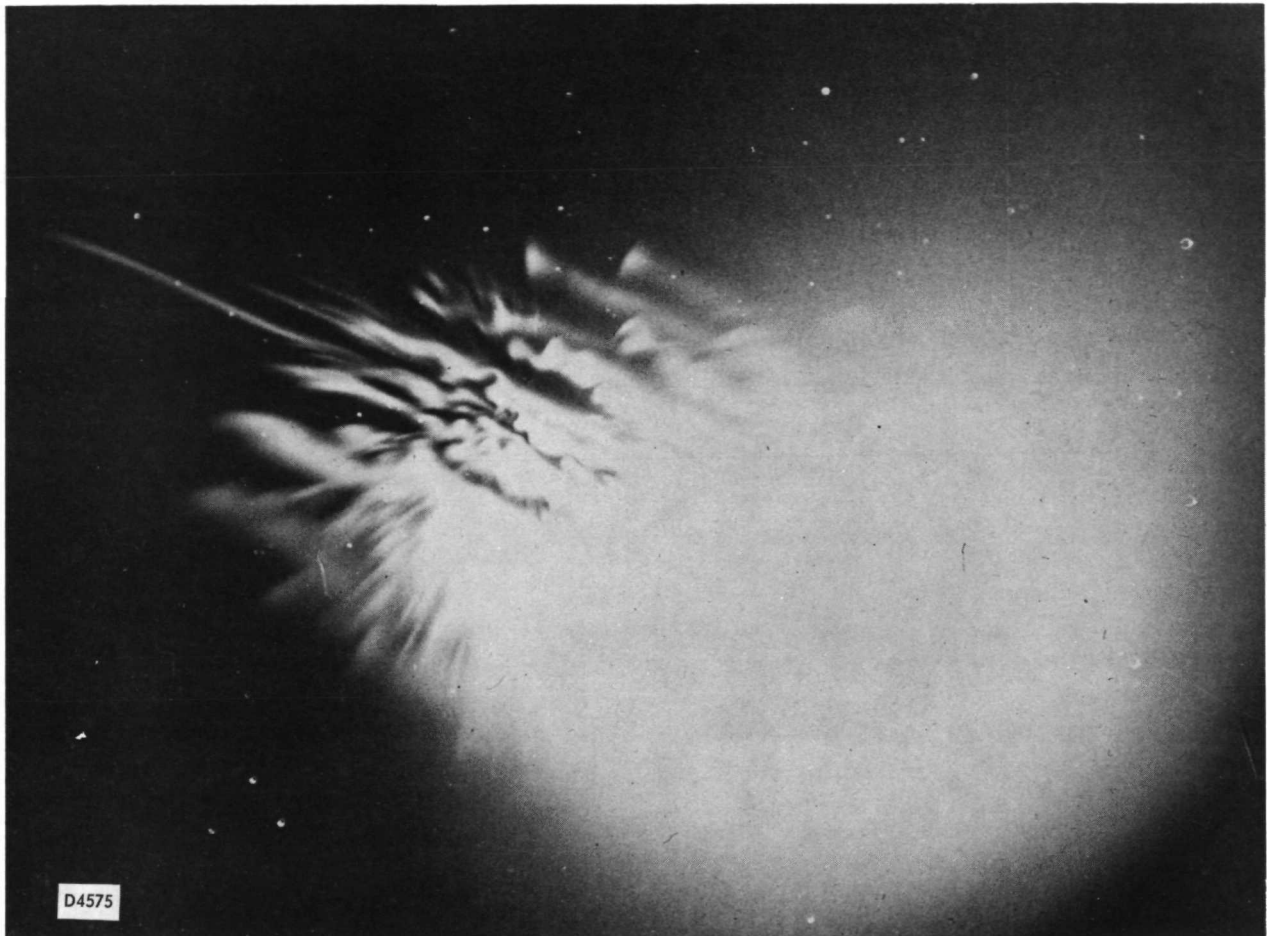


Fig. II. 11 Redwood Striations Viewed Directly Up the Magnetic Field Line (Technology International Corporation)



Fig. II. 12 Spruce Striations Viewed Directly Up the Magnetic Field Line (Technology International Corporation)

each of the other two clouds, then the wavelength for peak growth gives excellent agreement with the observed dominant widths.

SECTION II  
REFERENCES

1. NASA Final Report, Contract No. NASW-2040, March 1971.
2. N. J. Zabusky, F. W. Perkins, and J. H. Doles, III, J. Geophys. Res., 78, February 1973, Part I.
3. L. M. Linson and J. B. Workman, J. Geophys. Res., 75, 3211 (1970).
4. L. M. Linson, Plasma Cloud Striations, Avco Everett Research Laboratory, AMP 315, September 1970.
5. L. M. Linson and J. B. Workman, "Formation of Striations in Ionospheric Barium Ion Clouds," EOS: Trans., Am. Geophys. Union, 51, 396 (1970).
6. L. M. Linson, Nonlinear Barium Ion Cloud Dynamics, Trans., Am. Geophys. Union, 52, 298 April (1971).
7. L. M. Linson, Trans., Am. Geophys. Union, 52, 880 (December (1971).
8. L. M. Linson, Bull. Am. Phys. Soc., 17, 970 (1972).
9. G. Haerendel, R. Lust, and E. Rieger, Planet Space Sci., 15, 1 (1967).
10. N. J. Zabusky, F. W. Perkins, and J. H. Doles, III, J. Geophys. Res., 78, February 1973, Part II.
11. A. Simon and A. M. Sleeper, Barium Cloud Growth in a Highly Conducting Medium, J. Geophys. Res., 77, 2353 (1972).
12. A. Simon, J. Geophys. Res., 75, 6287 (1970).

### III. ION STREAMING INSTABILITIES WITH APPLICATION TO COLLISIONLESS SHOCK WAVE STRUCTURE

#### A. INTRODUCTION

The instabilities that result from the presence of two interpenetrating ion streams immersed in an electron background may provide the mechanism for collisionless momentum coupling between the two streams. The presence of a weak magnetic field can have a significant effect on the physical process. First, the magnetic field can inhibit the electrons from shorting out ion plasma oscillations for wavelengths long compared to the electron gyro-radius for propagation perpendicular to the magnetic field; second, gradients in the magnetic field give rise to electron currents that can drive ion acoustic waves unstable and increase the effective electron collision frequency; and third, whistler mode -- ion beam interactions are likely to be important, and the existence of whistler modes depends on the presence of a magnetic field.

The existence of collisionless plasma shock waves has provided the impetus for investigating mechanisms that can provide the anomalous dissipation that is required. Many experiments have shown that plasma turbulence is associated with these shock wave structures. Numerous linear plasma instabilities have been proposed as the mechanism that generates the observed turbulence. An overall review of the status of theoretical and experimental work in collisionless shock waves has been given by Friedman, et al.<sup>1</sup> We shall briefly review here the status of perpendicular,  $(\pi/2) - (m_e/m_i)^{1/2} < \theta < \pi/2$ , ( $\theta$  being the angle between

the flow direction and magnetic field) and oblique,  $0 \leq \Theta < (\pi/2) - (m_e/m_i)^{1/2}$  shock wave structures together with the different streaming instabilities and their possible roles in the formation of these structures. We shall then present an analysis of a new configuration leading to instability with possible application to parallel, intermediate Alfvén Mach number shocks.

For low  $\beta$ , perpendicular shocks, when  $T_e \gtrsim 5 - 10 T_i$ , a relative drift between the ions and electrons in excess of the ion acoustic speed can excite unstable ion acoustic waves.<sup>2,3</sup> The ensuing turbulent fluctuation spectrum  $\langle |\tilde{E}_k|^2 \rangle$  stochastically heats the electrons and the shock structure is controlled entirely by the electron resistivity associated with  $\langle |\tilde{E}_k|^2 \rangle$ . This kind of shock structure can be oscillatory or monotonic (depending on the amount of turbulent dissipation) and it exists as long as the downstream plasma flow velocity,  $V_2$ , is greater than or equal to the downstream ion acoustic speed,  $C_{S2}$ . When  $V_2 < C_{S2}$  (corresponding to an upstream Alfvén Mach number  $M_{A1} > M^* = 2.76$ ), a narrow gasdynamic subshock is embedded in the magnetic shock layer.<sup>4</sup> At these higher upstream flow velocities, it is the presence of ion viscous dissipation dominating (only) the subshock structure that provides the requisite degradation of the additional directed energy into thermal energy.

Recent studies by Papadopoulos et al<sup>5</sup> suggest that two ion beams counterstreaming in a background rest frame of cool magnetized electrons can also effectively couple momentum from one stream to the other at characteristic frequencies and growth rates comparable with the lower hybrid frequency. This instability is operative only if the Alfvén Mach number,  $M_d$ , for the relative drift between the ion streams satisfies the inequality

$$M_d < 2(1 + \beta_e)^{1/2}. \quad (\text{III-1})$$

and if the streaming direction is nearly perpendicular to the magnetic field. We shall introduce the concept that the relative drift is the difference between the upstream and downstream velocities,  $V_1$  and  $V_2$ , respectively, i. e.  $V_d = V_1 - V_2$ . If we define the Alfvén Mach number in terms of the local value of the Alfvén velocity which varies as  $B/n^{1/2}$ , we can express the limitation implied by Eq. (III-1) in terms of the upstream Mach number,  $M_{A1} = V_1/C_{A1}$ . For instance, in the case of a low  $\beta$ , perpendicular shock structure with the interaction region taken to be the center of the shock layer so that  $\beta(x) \sim 1$ ,  $n(x) \sim (1/2)(n_1 + n_2)$ , it can be shown that

$$2(2)^{1/2} > M_d(x) = M_{A1} \left( \frac{2}{1+\tau} \right)^{1/2} \frac{\tau-1}{\tau} \quad (\text{III-2})$$

where  $\tau = n_2/n_1$  is the density compression ratio. By assuming  $\gamma = 5/3$ ,  $\tau$  may be related to the shock Alfvén Mach number  $M_{A1}$  through the relation

$$\tau = \frac{1}{2} \sqrt{25 + 52 M_{A1}^2 + 4M_{A1}^4} - \frac{5}{2} - M_{A1}^2, \quad (\text{III-3})$$

valid only when the unshocked plasma is cold. Thus, from Eqs. (III-2) and (III-3) this magnetized ion-ion instability can operate only for  $M_{A1} < 6$ .

The "modified" two stream instability<sup>6, 7</sup> has also been proposed for nearly perpendicular shocks. This instability is driven by relative streaming of ions and electrons across a magnetic field. It is so named because its dispersion relation, in the fluid limit, is similar to that for the Buneman two-stream instability<sup>8</sup>. Unlike the ion acoustic instability which selectively

heats electrons, the "modified" two-stream instability produces large and comparable ion and electron heating. Like the magnetic ion-ion interaction discussed in the previous paragraph, the characteristic frequency and growth rate for the modified instability is comparable to the lower hybrid frequency and it is operative only if the Alfvén Mach number for the relative drift between the ions and electrons satisfies the inequality,

$$M_d < (1 + \beta_e)^{1/2}.$$

Significant among recent advances in the area of magnetic streaming instabilities and their applications to oblique shock structures in collisionless plasmas are the beam-whistler (BW)<sup>9</sup> and beam-cyclotron (BC)<sup>10,11</sup> instabilities. These are characterized by strong interactions between one of the two counterstreaming ion acoustic beam modes and the whistler or electron cyclotron mode (see Fig. III.1). While the BC instability does result in electron heating, it nevertheless is inadequate as a mechanism for ion-ion momentum coupling. Here the electron cyclotron modes are heavily damped and do not interact with the beam modes. On the other hand, BW instabilities, operative in the range  $0 < \Theta < (\pi/2)$  and  $M_d \lesssim (m_i/m_e)^{1/2} \times \cos \Theta$ , do result in turbulence which can suitably couple the two ion beams. Clearly, the application of BW interactions to oblique shock structure is especially attractive since they are operative over a substantially larger range of shock Mach numbers than are the magnetic counterstreaming ion-ion and modified two stream instabilities discussed earlier.

We now briefly review the oblique collisionless shock structure study of Lindeman and Drummond.<sup>9</sup> Their analysis points to the existence of four critical Mach numbers  $M^*$ ,  $M^{**}$ ,  $M^{***}$ ,  $M^{****}$ . The first of these, cited earlier for perpendicular shocks, is the value of the upstream Alfvén Mach

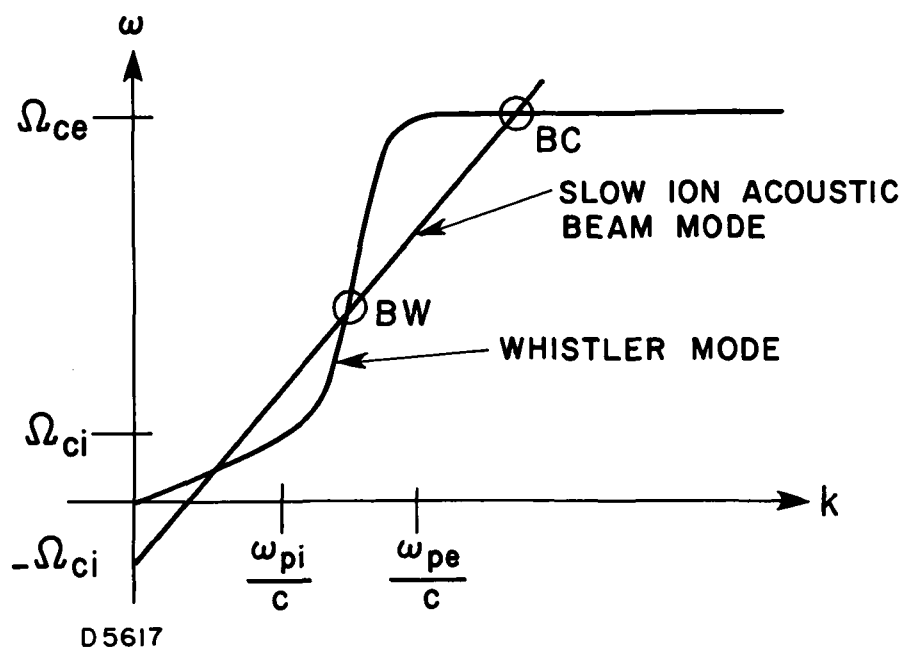


Fig. III. 1 Schematic of the Dispersion Relation Showing the Interaction Regions Leading to Beam-Cyclotron (BC) and Beam-Whistler (BW) Instabilities.

number  $M_{A1}$  for which the downstream flow velocity equals the ion acoustic speed. When  $M_{A1} < M^*$ , the shock structure is a large amplitude whistler (in the rest frame of the shock front). The damping of the whistler and subsequent electron heating are brought about by the anomalous resistivity. When  $M_{A1} > M^*$ , a nonmagnetic subshock appears downstream of the whistler region. It was found, however, that this subshock is a single large amplitude ion acoustic wave of scale length of order of the Debeye length; this refutes the usual notion of the anomalous ion viscosity as a broadening mechanism for subshocks. When  $M_{A1} > M^{**}$ , a fraction of the incoming ions is reflected from the potential barrier of the ion acoustic wave. These reflected ions then interact with the counterstreaming upstream ions through a BW instability resulting in pickup and heating of the reflected ions by the incoming ions. Since the relative drift velocity between the incoming and reflected particles  $\approx 2V$ , Lindeman and Drummond<sup>9</sup> predict a third critical Mach number  $M^{***} = 0.5 (m_i/2m_e)^{1/2} \cos \theta$ , such that for  $M_{A1} > M^{***}$ , the above BW instability which couples the counterstreaming ions is inoperative. Finally, when  $M > M^{****} = 0.5(m_i/m_e)^{1/2} \cos \theta$ , the whistler can no longer stand in the shock layer (in the rest frame of the shock) so that its structure is completely dominated by the ion acoustic mode.

It is interesting to note that for parallel propagation ( $k \parallel B_0$ ), the ion acoustic modes of the counterstreaming ions uncouple from the whistler mode so that in the assumed frequency range  $\Omega_{ci} \ll |\omega|$ ,  $|\omega - kU| \ll \Omega_{ce}$  of Lindeman and Drummond,<sup>9</sup> the BW instability no longer exists. On the other hand, if one relaxes the frequency restriction to lower frequencies, i.e.  $0 \lesssim |\omega|$ ,  $|\omega - kU| \ll \Omega_{ce}$ , then even in the case of parallel propagation a beam mode can, in fact, enter into unstable interaction with the

with the whistler leading to coupling of the two ion beams. This problem and its application to parallel shock wave structure are the topics of central interest in this report. While our analysis is restrictive inasmuch as we concentrate only on the  $\underline{k} \parallel \underline{B}_0$ ,  $\underline{V} \parallel \underline{B}_0$  case, it is nevertheless useful to know if ion dissipation can be generated.

In Section III. B, we analyze the linear instability of two counterstreaming ion beams in the presence of magnetized electrons; here, the analysis is carried out in the rest frame of the electrons. In Section III. C we analyze the resulting dispersion relation in the rest frame of the parallel shock at different upstream Mach numbers and at different stations in the shock layer. The result of this analysis is a map showing the range of Mach numbers as a function of position into the shock for which unstable waves can stand inside the shock.

## B. LINEAR THEORY

We analyze here the instability arising in a collisionless plasma configuration consisting of two ion beams counterstreaming along the magnetic field ( $\underline{V}_s \parallel \underline{B}_0$ ) through an electron background.  $\underline{V}_s$  represents the streaming velocity of  $s^{\text{th}}$  species of ions. The ion and electron motions are modeled by fluid equations valid for wavelengths long compared with the electron gyroradius. Restricting ourselves to the case of parallel propagation ( $\underline{k} \parallel \underline{B}_0$ ), the appropriate electromagnetic dispersion relation then has the form:

$$\frac{k_c^2}{\omega^2} - \epsilon_{11}(\underline{k}, \omega) = \pm i\epsilon_{12}(\underline{k}, \omega), \quad (\text{III-4})$$

where, in the electron rest frame,

$$\epsilon_{11}(\underline{k}, \omega) = 1 - \frac{\omega_{pe}^2}{\omega^2 - \Omega_{ce}^2} - \sum_{\substack{s=1, 2 \\ (\text{ions})}} \frac{(\omega_{ps}/\omega^2)(\omega - \underline{k} \cdot \underline{v}_s)^2}{(\omega - \underline{k} \cdot \underline{v}_s)^2 - \Omega_{ci}^2} \quad (\text{III-5a})$$

and

$$\epsilon_{12}(\underline{k}, \omega) = \frac{i\omega_{pe}^2 \Omega_{ce}}{\omega(\omega^2 - \Omega_{ce}^2)} - \sum_{\substack{s=1, 2 \\ (\text{ions})}} \frac{i(\omega_{ps}/\omega^2)(\omega - \underline{k} \cdot \underline{v}_s) \Omega_{ci}}{(\omega - \underline{k} \cdot \underline{v}_s)^2 - \Omega_{ci}^2} \quad (\text{III-5b})$$

$\Omega_{ci} = Z |e| B_o / m_i$ ,  $\Omega_{ce} = |e| B_o / m_e$  deonoting the ion and electron cyclotron frequencies and  $\omega_{ps}$ ,  $\omega_{pe}$  the  $s^{\text{th}}$  ion beam ( $s = 1, 2$ ) and electron plasma frequencies, respectively. We note that within the fluid approximation, the dispersion relation Eq. (III-4) is unaffected by the presence of electron thermal pressure since the thermal velocity does not appear in the 11, 22, and 12 components of the dielectric tensor in the fluid limit for the case of parallel propagation.

We now make the low frequency approximations that 1) the displacement current is negligibly small ( $\omega \ll k_c$ ), and 2) the electrons have zero mass ( $|\omega| \ll \Omega_{ce}, \omega_{pe}$ ). Introducing the dimensionless densities  $\delta = Zn_2/n_e$ ,  $(1 - \delta) = Zn_1/n_e$  (it is understood that the composite ion beams-electron plasma system is charge neutral), the dispersion relation simplifies to

$$\frac{k_c^2 c^2}{\omega_{pi}^2} + \frac{\omega}{\Omega_{ci}} + \frac{(1 - \delta)(\omega - \underline{k} \cdot \underline{v}_1)}{\omega - \underline{k} \cdot \underline{v}_1 \pm \Omega_{ci}} + \frac{\delta(\omega - \underline{k} \cdot \underline{v}_2)}{\omega - \underline{k} \cdot \underline{v}_2 \pm \Omega_{ci}} = 0 \quad (\text{III-6a, b})$$

where Eq. (III-6a) refers to the upper signs, and Eq. (III-6b) refers to the lower signs. We also apply the zero current constraint

$$(1 - \delta) \underline{V}_1 + \delta \underline{V}_2 = 0. \quad (\text{III-7})$$

For the low frequency case under consideration here, it is crucial that condition (III-7) be met for arbitrary beam strength ( $0 \leq \delta \leq 1$ ) (see Ref. 12). In the sequel, Eq. (III-6b) corresponding to the lower sign, can be dropped from further consideration since it is identical to Eq. (III-6a) with  $\omega \rightarrow -\omega$  and  $\underline{k} \rightarrow -\underline{k}$ . It is convenient to introduce here the relative drift velocity  $\underline{U} = \underline{V}_2 - \underline{V}_1$ , so that from Eq. (III-7),  $\underline{V}_1 = -\delta \underline{U}$ ,  $\underline{V}_2 = (1 - \delta)\underline{U}$ , and Eq. (III-6a) can be simplified to

$$\frac{\frac{k^2 c}{\omega_{pi}^2} - \frac{\omega}{\Omega_{ci}} + 1 - \frac{(1 - \delta) \Omega_{ci}}{\omega + \delta \underline{k} \cdot \underline{U} + \Omega_{ci}} - \frac{\delta \Omega_{ci}}{\omega - (1 - \delta) \underline{k} \cdot \underline{U} + \Omega_{ci}}}{= 0.} \quad (\text{III-8})$$

Now, for  $0 \leq \delta < 0.5$ , it is clear that ion stream 1 has more the role of "plasma" while 2 has more the role of "beam". When  $0.5 \leq \delta \leq 1$ , these roles are interchanged. Since, however, the corresponding interchanges

$$\delta \longleftrightarrow (1 - \delta), \quad \underline{k} \cdot \underline{U} \longleftrightarrow -\underline{k} \cdot \underline{U}$$

leave Eq. (III-8) unchanged, analysis of the range  $0.5 \leq \delta \leq 1.0$  would be redundant. It is therefore sufficient to investigate only  $0 \leq \delta \leq 0.5$ .

For given values of the parameter  $\delta$  and  $M_d = U/C_A$  (it is convenient to normalize  $U$  with respect to the Alfvén speed  $C_A$ ), our task consists in solving Eq. (III-8) for  $\omega = \omega(k)$ ; here  $k$  is considered to be real and  $\omega$  can be real or complex. Since Eq. (III-8) is a cubic equation in  $\omega$  with real coefficients for real  $k$ , complex roots necessarily occur in conjugate pairs.

Hence, whenever a growing mode ( $\text{Im } \omega > 0$ ) is present, there is also a decaying mode ( $\text{Im } \omega < 0$ ).

For  $\delta = 0$ , one recovers the usual whistler ( $W_{\pm}$ ) and ion-cyclotron ( $IC_{\pm}$ ) dispersion branches given analytically by

$$\omega_{\pm} = k^2 C_A^2 / 2 \Omega_{ci} \pm k C_A (1 + k^2 C_A^2 / 4 \Omega_{ci}^2)^{1/2} \quad (\text{III-9})$$

For weak beams ( $\delta \ll 1$ ), the intersection points P, Q, R (see Fig. III-2) between the ion beam mode

$$\omega = (1 - \delta)kU - \Omega_{ci} \quad (\text{III-10})$$

and the  $W_{+}$  and  $IC_{-}$  branches of Eq. (III-9) suggest possible strong interactions near these points. Indeed Kovner's analysis<sup>13</sup> shows that beam - $IC_{-}$  interaction is stable while the beam -  $W_{+}$  interactions are unstable with growth rates

$$\gamma_{\ell} = \frac{\delta^{1/2} \Omega_{ci} k_{\ell} U}{(k_{\ell}^2 U^2 - \Omega_{ci}^2)^{1/2}} \quad (\ell = P, Q), \quad (\text{III-11})$$

where, from Eqs. (III-9) and (III-10),  $k_P$  and  $k_Q$  depend on the slope ( $= M_d$ ) of the beam line. Note that the beam-cyclotron (BC) intersection shown in Fig. III.1 does not appear in Fig. III.2 due to our approximation  $m_e \rightarrow 0$ .

We have extended Kovner's weak beam study by solving Eq. (III-8) for arbitrary values of  $\delta$  ( $0 \leq \delta \leq 0.5$ ). By expanding the dispersion relation (III-8) for small  $k$ , one readily finds

$$\text{Im } \omega = k C_A \left[ \delta (1 - \delta) M_d^2 - 1 \right]^{1/2}, \quad (\text{III-12})$$

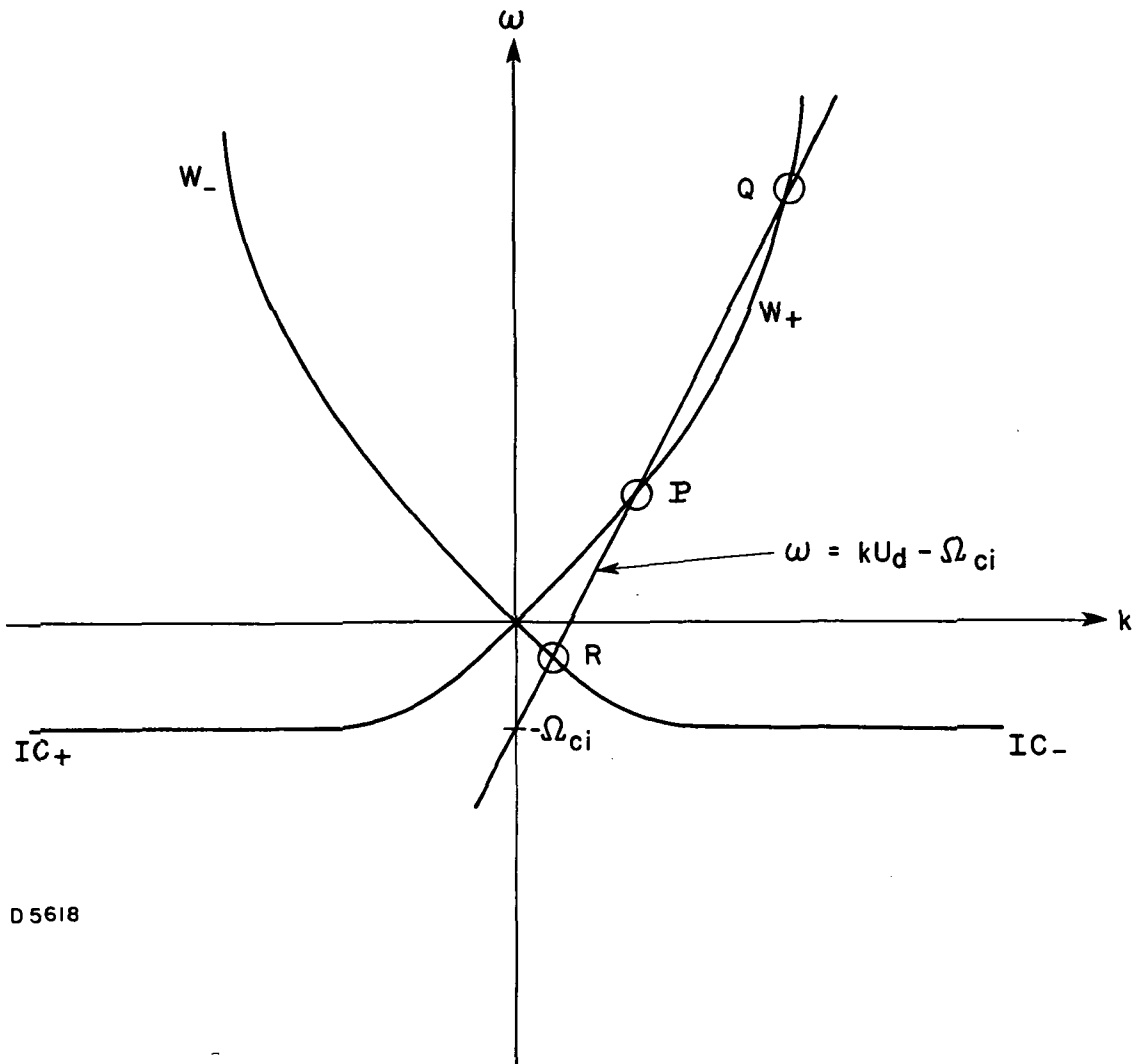


Fig. III. 2 Superposition of the Whistler ( $W_+$ ) and Ion Cyclotron ( $IC_+$ ) Modes for  $\delta = 0$  with a Weak Beam Mode. The intersection points R, P, and Q represent regions where strong interactions can occur.

so that these long wavelength modes are unstable only if

$$M_d > \frac{1}{[\delta(1-\delta)]^{1/2}} \quad (III-13)$$

This condition is thus sufficient for instability, but is not necessary as we shall see below. We should emphasize that due to the application of the condition (III-7), we are dealing only with zero-current instabilities and thus the stronger, current-driven instabilities often treated are excluded. It is easy to show that there must be complex roots of Eq. (III-8) for values of  $k$  and  $U$  determined by setting  $\omega$  given by Eq. (III-10) equal to  $\omega_+$  given by Eq. (III-9). The resulting relationship between  $U$  and  $k$  is

$$U = \frac{\Omega_{ci}}{(1-\delta)k} \left[ 1 + \frac{k^2 C_A^2}{\Omega_{ci}^2} + \frac{k C_A}{\Omega_{ci}} (1 + k^2 C_A^2 / 4\Omega_{ci}^2)^{1/2} \right]. \quad (III-14)$$

By appropriate manipulation, Eq. (III-8) can be brought into the form

$$(\omega + \delta k U + \Omega_{ci})(\omega - \omega_-)(\omega - \omega_+)(\omega - (1-\delta)k U + \Omega_{ci}) = -\delta(1-\delta)\Omega_{ci}^2 k^2 U^2. \quad (III-15)$$

where we have introduced a fourth, extraneous root,  $\omega = -\Omega_{ci}$ , in order to produce the above quartic equation in  $\omega$ . When Eq. (III-14) is satisfied, the third and fourth factors on the lefthand side of Eq. (III-15) are identical and hence positive for real  $\omega$ . The righthand side is always negative while the lefthand side is negative only for  $-\delta k U - \Omega_{ci} < \omega < \omega_- < 0$ . In this range there is only one real root,  $\omega_1$ , such that  $-\delta k U - \Omega_{ci} < \omega_1 < -\Omega_{ci}$ ; in addition to the extraneous root at  $-\Omega_{ci}$ . Hence the other two roots of

Eq. (III-15) and thus Eq. (III-8) are complex for  $k$  and  $U$  determined by Eq. (III-14).

Dispersion curves obtained from Eq. (III-8) are displayed in Figs. III.3a - III.3d for values of  $\delta = 0.1$  and  $0.5$  and drift Mach numbers  $M_d = 3$  and  $7$ . Note that  $kU$  has been taken to be negative here as opposed to the positive value shown in Fig. III.2. We find that for  $\delta = 0.1$ , the peak growth rate increases only slightly from  $\gamma \approx 0.32 \Omega_{ci}$  at  $M_d = 3$  to  $\gamma \approx 0.38 \Omega_{ci}$  at  $M_d = 7$ , while for  $\delta = 0.5$ , the peak growth rate increases more markedly with  $M_d$ , rising from  $\gamma = 0.34 \Omega_{ci}$  at  $M_d = 3$  to  $\gamma = 0.72 \Omega_{ci}$  at  $M_d = 7$ . Note that for  $\delta = 0.5$ , the dispersion curves are symmetric in  $k$  as it is impossible to distinguish the beam from the plasma while for  $\delta = 0.1$  the beam-like mode can be clearly identified. Also note that in Fig. III.3a the region near  $k = 0$  is stable in agreement with Eq. (III-13) but that there is instability for a finite range of negative  $k$ .

The regions of instability in  $k$ ,  $U$  space for  $\delta = 0.1$  and  $0.5$ , obtained by setting the discriminant of Eq. (III-8) equal to zero, are shown in Figs. III.4a and III.4b respectively. Also shown by dashed lines is the generalization for arbitrary  $\delta$  of the "Kovner" lines given by Eq. (III-14). These dashed lines, which correspond to the intersection points  $P$  and  $Q$  in Fig. III.2, were shown above to always lie in the region of instability. It is easy to determine that the minimum in the dashed line occurs at  $k C_A / \Omega_{ci} = (4/3)^{1/2} \sim 1.15$  for which

$$M_d = \frac{3(3)^{1/2}}{2(1-\delta)} \sim \frac{2.6}{1-\delta}. \quad (\text{III-16})$$

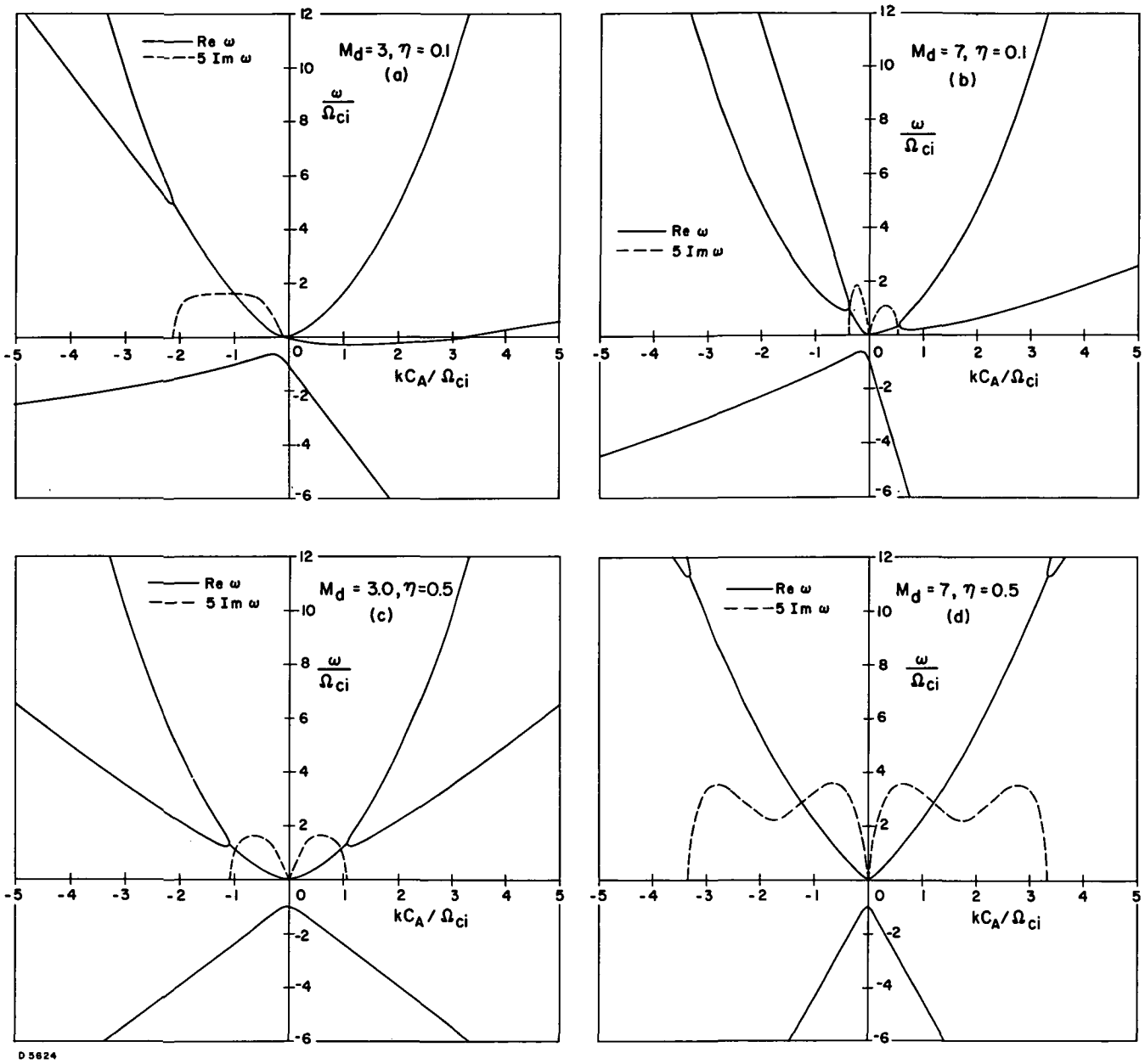


Fig. III.3 The Dispersion Relation (III.8) for: a)  $\delta = 0.1$ ,  $M_d = 3$ ; b)  $\delta = 0.1$ ,  $M_d = 7$ ; c)  $\delta = 0.5$ ,  $M_d = 3$ ; d)  $\delta = 0.5$ ,  $M_d = 7$ .

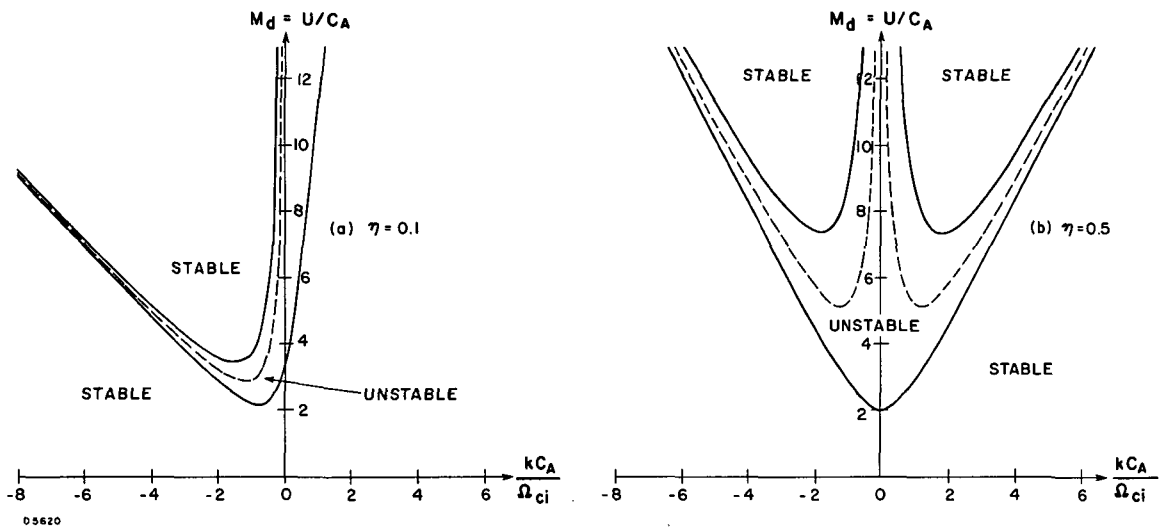


Fig. III.4 Range of Unstable Values of  $k$  as a Function of Relative Drift Velocity for a)  $\delta = 0.1$  and b)  $\delta = 0.5$ .

This value corresponds to the relative drift such that the beam line Fig. III.2 is tangent to the  $W_+$  branch, i. e., the points P and Q coalesce. For larger values of drift there are two peaks in the spectrum of unstable  $k$ . Figure III.4a shows that for  $M_d > 3.5$ , there are two discrete ranges of  $k$  which are unstable. For large drift ( $M_d \rightarrow \infty$ ) there are unstable modes for  $k$  in the range

$$\left| (1 - \delta) M_d - \frac{2}{M_d(1 - \delta^{1/2})} \right| < \left| \frac{kC_a}{\Omega_{ci}} \right| < \left| (1 - \delta) M_d - \frac{2}{M_d(1 + \delta^{1/2})} \right| \quad (\text{III-17})$$

The width of this unstable spectrum is thus

$$\Delta k \sim \frac{4 \delta^{1/2}}{(1 - \delta) U} \Omega_{ci} \quad (\text{III-16})$$

and the peak growth rate is given approximately by  $\text{Im}\omega \sim \delta^{1/2} \Omega_{ci}$ . These expressions are in agreement with the numerical results shown in Figs. III.3 and III.4.

### C. RELEVANCE FOR SHOCK WAVE STRUCTURE

The purpose of this section is to determine when the unstable whistlers analyzed in Section III-B can grow to large amplitude inside a shock front propagating along the magnetic field. Hence, in addition to being unstable we shall apply the requirement that the growing wave should have zero group velocity in the shock frame. The group velocity of the wave is not only a function of  $\omega$  and  $k$ , but also of the position in the shock front as we shall see below. Waves with zero group velocity can be expected to remain in the unstable region for a sufficiently long time to reach large amplitude

and generate turbulence. We consider only parallel shock waves for which the sound speed  $C_{SO} = (\gamma K(T_e + T_i)/m_i)^{1/2}$  and the Alfvén speed  $C_{AO} = (B_o^2/\mu_0 \rho_i)^{1/2}$  in the unshocked gas are equal. Thus our study excludes any consideration of "switch-on" shocks that occur for  $C_{SO} < C_{AO}$ ; here the external magnetic field remains constant and parallel to the direction of plasma flow across the shock layer.

In the rest frame of the shock front, the ions are modeled as a linear combination of the upstream ( $u$ ) and downstream ( $d$ ) velocity distribution functions, i. e.

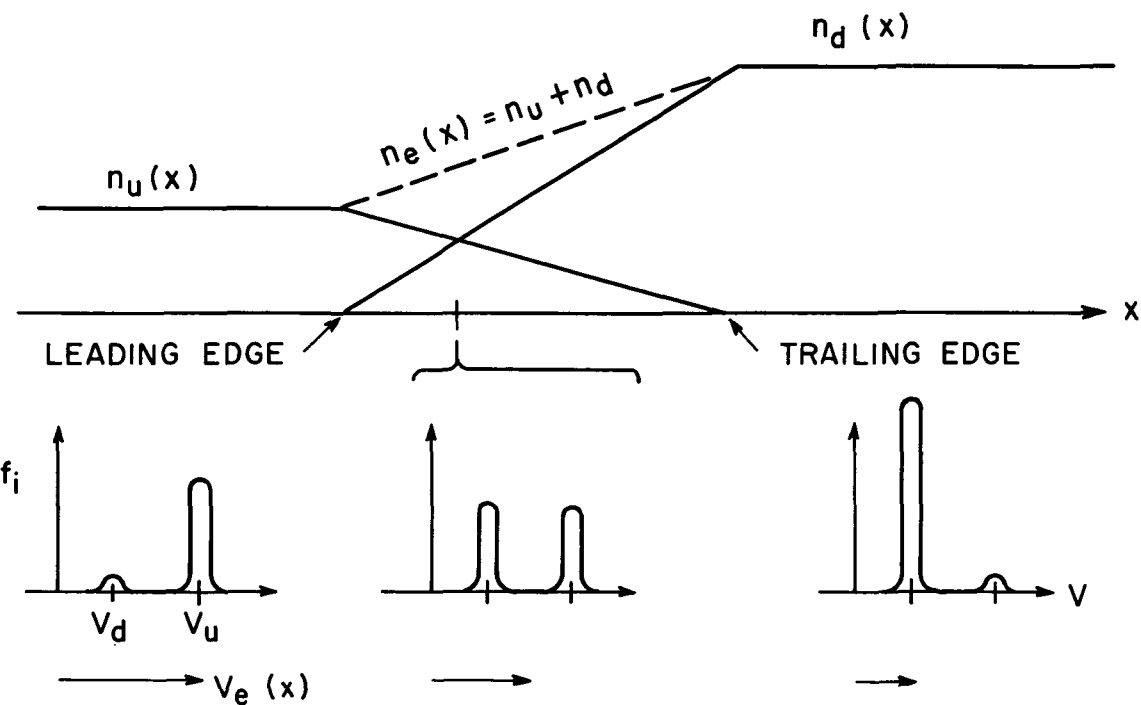
$$f(\underline{x}, \underline{v}) = n_u(\underline{x}) \delta(\underline{v} - \underline{v}_u) + n_d(\underline{x}) \delta(\underline{v} - \underline{v}_d). \quad (III-18)$$

$n_u(\underline{x})$  is taken to decrease linearly from its upstream value at the leading edge of the shock to zero at the trailing edge while  $n_d(\underline{x})$  increases linearly from zero at the leading edge to its downstream value at the trailing edge as indicated schematically in Fig. III.5. The electrons, on the other hand, are modeled as a single fluid moving with an average drift velocity,  $\underline{V}_e(\underline{x})$  determined by the zero current condition

$$\underline{V}_e(\underline{x}) = (1 - \delta(\underline{x})) \underline{v}_u + \delta(\underline{x}) \underline{v}_d \quad (III-19)$$

where the fraction of the total density represented by the downstream species,  $\delta(\underline{x})$ , is now a function of position through the shock.

In this section the dispersion relation (III-8) is analyzed in the shock frame. The primary difference from the previous section is that the real part of the frequency is doppler shifted by the amount  $\underline{k} \cdot \underline{V}_e(\underline{x})$  which is a function of position in the shock. The instability properties are unchanged and depend only on the relative drift  $\underline{U} = \underline{v}_d - \underline{v}_u$  (which is independent of position in the shock) and  $\delta(\underline{x})$  (which is dependent on the position in the shock).



D 5621

Fig. III. 5 Sketch of the Ion Velocity Distribution Function Indicating the Assumed Linear Variation Through the Shock.

The group velocity, defined as  $\partial \omega_s' / \partial k$  where  $\omega_s'$  is the real part of the frequency  $\omega_s$  in the shock frame (equal to  $\omega + \underline{k} \cdot \underline{V}(x)$ ), also depends on the position within the shock.

In the previous section, dispersion curves and stability criteria were given in terms of the relative drift velocity,  $U$ , of the two ion streams or, more exactly, the relative drift Alfvén Mach number,  $M_d = U/C_A$ , where  $C_A = B_0(z/\mu_0 m_i n_e)^{1/2}$  is the local Alfvén velocity. In this section we shall specify these properties and criteria in terms of the upstream Alfvén Mach number,  $M_A = V_u/C_{AO}$ , and the fraction of the distance,  $\zeta$ , through the shock. From Eq. (III-18) we have

$$n_e(x) = (1 - \zeta)n_{uo} + \zeta n_{do} \quad (\text{III-20})$$

where  $n_{uo}$  and  $n_{do}$  represent the unshocked, upstream density and shocked, downstream density respectively. Thus

$$\zeta = \frac{\delta}{[\delta + \tau(1 - \delta)]} \quad (\text{III-21})$$

where  $\tau = n_{do}/n_{uo}$  is the compression ratio across the shock determined by the Rankine-Hugoniot relations;

$$\tau = \frac{(\gamma + 1) M_A^2}{(\gamma - 1) M_A^2 + 2} = \frac{4 M_A^2}{M_A^2 + 3} \quad (\text{for } \gamma = 5/3) \quad (\text{III-22})$$

when it is remembered that we have assumed  $\beta \sim 1$  so that the upstream acoustic speed and Alfvén speed are equal. The local Alfvén velocity decreases through the shock as the plasma density increases;

$$C_A = C_{AO} \left[ \frac{M_A^2 + 3}{M_A^2 + 3 + 3\zeta(M_A^2 - 1)} \right]^{1/2} \quad (III-23)$$

For a given upstream Mach number,  $M_A$ , the local drift Mach number is given by

$$M_d = \frac{V_u - V_d}{C_A} = \frac{3(M_A^2 - 1)}{4M_A^2} \left( 1 + \frac{3\zeta(M_A^2 - 1)}{M_A^2 + 3} \right)^{1/2} \quad (III-24)$$

Solutions of the dispersion relation (III-8) in the shock frame are shown in Figs. III.6a through III.6d for the same values of  $\delta$  and  $M_d$  shown in Figs. III.3a through III.3d. Note that the wavenumber scale in Figs. III.6 are normalized using the upstream Alfvén velocity  $C_{AO}$  instead of the local value. The shape of the unstable spectrum is unchanged. The real frequencies for the case  $\delta = 0.5$  are no longer symmetric about  $k = 0$  due to the doppler shift. Note that the group velocity does not equal zero (solid line with zero slope) for any of the values of  $k$  that are unstable in these particular cases. The case for  $\delta = 0.1$  and  $M_A = 4.1$  has the smallest group velocity. The values of Alfvén Mach number shown are obtained by inverting Eqs. (III-21) and (III-24).

Figures III.7a and III.7b present the range of unstable wave numbers as a function of the upstream Alfvén Mach number,  $M_A$ , at two different positions within the shock front. These figures are different from their counterparts in Figs. III.4a and III.4b since the value of  $\delta$  varies for different values of  $M_A$  because  $\zeta$ , the position within the shock is held fixed. We see that near the front of the shock there is a wide range of unstable wavenumbers for  $M_A \gtrsim 3$ . The growth rate is of the order of

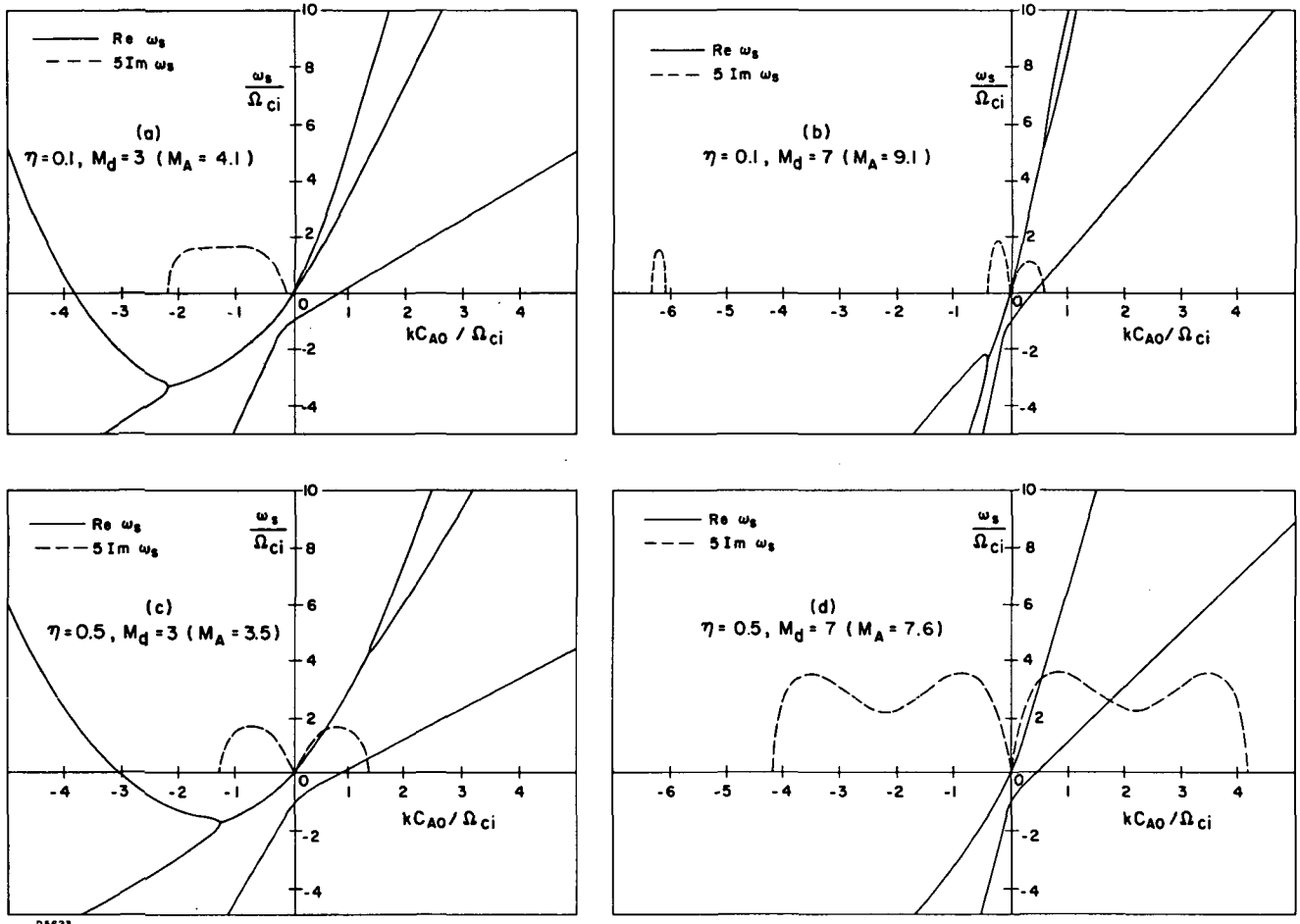


Fig. III. 6 The Dispersion Relation III. 8 in the Shock Frame for the Four Cases Shown in Fig. III. 3 Where  $\omega_s = \omega + \mathbf{k} \cdot \mathbf{V}_e$ .

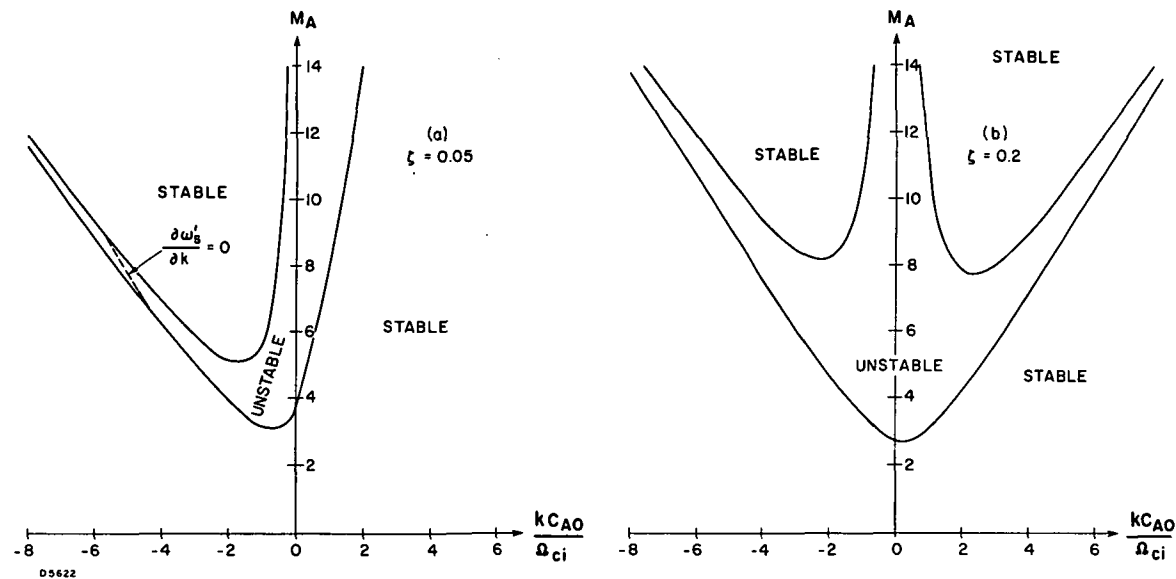


Fig. III.7 Range of Unstable Wavenumbers as a Function of Upstream Alfvén Mach Number at Two Positions within the Front at a)  $\zeta = 0.05$  and b)  $\zeta = 0.2$ . The dashed line corresponds to values of  $k$  for which the group velocity of unstable waves is zero in the shock front.

$\Omega_{ci}$ . However, most of these waves have positive group velocities and are swept downstream with the flow before they have had a chance to grow significantly. Only unstable waves with nearly zero group velocity can be expected to grow to large amplitude. In Fig. III.7a, the values of  $k$  for zero group velocity waves in the unstable region are shown by a dashed line. Thus, Mach numbers in the range  $6.8 < M_A < 9.1$  should be able to produce turbulence at  $\zeta > 0.05$  according to the linearized analysis presented here. Such waves don't exist for the parameter ranges shown in Fig. III.7b at  $\zeta > 0.2$ .

Figure III.8 shows the range of upstream Alfvén Mach numbers for which unstable whistlers will stand in the shock as a function of distance into the shock. Two immediate conclusions can be made. The first is that this mechanism can only be important for  $M_A > 5.5$ . The second is that these waves are confined to the leading edge of the shock; unstable waves near the middle or trailing edge will be swept downstream. This result is in agreement with laboratory experiments<sup>15</sup> that measured magnetic field fluctuations in lower Mach number shock waves.

#### D. SUMMARY

We have derived the electromagnetic dispersion relation for two counterstreaming ion beams in a stationary electron background. The dispersion relation which is unaffected by electron pressure terms in the fluid approximation has been solved numerically to find the regions of instability in the  $k - M_d$  space. It is found that for beam-whistler modes to be unstable, it is necessary that the relative drift Mach number be greater than 2.0 although this condition is not sufficient for instability.

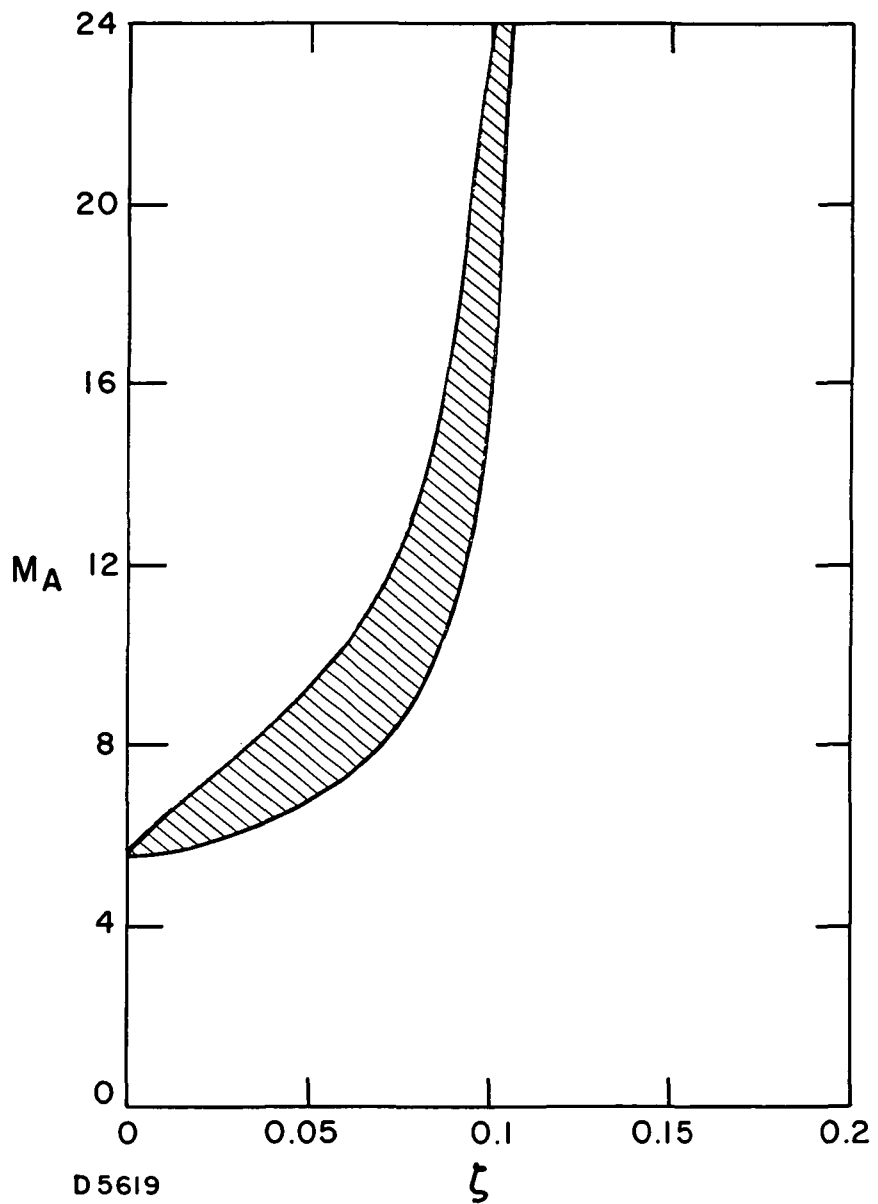


Fig. III. 8 Range of Alfvén Mach Numbers for Which Unstable Whistlers will Stand in the Shock as a Function of Position Within the Shock.

The bandwidth of  $k$  over which the unstable modes exist is shown to decrease inversely with the relative drift velocity for large relative drift velocities.

By modeling the shock structure in a Mott-Smith formalism as consisting of streaming up-stream and down-stream ions, the linear analysis was applied to the study of shock wave structure propagating along the magnetic field. Invoking the criterion that only unstable waves with zero group velocity will have time to grow within the shock thickness, we found the range of Mach numbers for which some unstable beam-whistler modes could grow to large amplitudes. We suggest that this may be a possible mechanism to generate turbulence that many experiments have shown to be associated with the shock wave structures. The plasma turbulence in turn can provide the explanation for anomalous dissipation. However, in our model, the unstable beam-whistler modes can stand near the leading edge of the shock only for upstream Mach numbers greater than 5.5.

The most serious limitation of the present analysis is the restriction  $k \parallel B$ . For waves propagating at an angle to the magnetic field, the dispersion relation becomes much more complicated and electron thermal effects have a significant interaction with the magnetic modes treated here. The analysis presented here ought to be extended to include the stability properties of these obliquely propagating waves. The assumption of cold ions ought to be relaxed particularly since one of the ion species in this study has been taken to be the shocked ions. Ion thermal effects could have a significant effect on the stability properties of counter-streaming ion beams. As a final comment, it should be emphasized that this instability depends on having included the effect of the magnetic field on the ions. If  $\Omega_{ci} \rightarrow 0$  in Eq. (III. 8), the instability disappears.

SECTION III  
REFERENCES

1. H. W. Friedman, L. M. Linson, R. M. Patrick, and H. E. Petschek, Collisionless Shocks in Plasmas, Annual Review of Fluid Mechanics, 3, 63 (1971).
2. J. D. Jackson, Plasma Phys. (J. Nucl. Energy, Part C), 1, 171 (1960).
3. T. E. Stringer, J. Nucl. Energy Part C, 6, 267 (1964).
4. P. Germain, A Model of Some Plasma Shock Structures in Proc. Symposia in Applied Mathematics, Vol. XVIII, 17-45, (Grad, H., Ed., American Mathematical Society, Providence, R. I., 1967).
5. K. Papadopoulos, R. C. Davidson, J. M. Dawson, I. Haber, D. A. Hammer, N. A. Krall, and R. Shanny, Phys. Fluids, 14, 849 (1971).
6. J. B. McBride, and E. Ott, Electromagnetic and Finite  $\beta_e$  Effects on the Modified Two-Stream Instability, NRL Memorandum Report 2366 (October 1971).
7. J. B. McBride, E. Ott, J. P. Boris, and J. H. Orens, Theory and Simulation of Turbulent Heating by the Modified Two-Stream Instability NRL Memorandum Report 2428 (April 1972).
8. O. Buneman, J. Nucl. Energy, Part C, 4, 111 (1961).
9. E. L. Lindeman, and W. F. Drummond, Studies of Oblique Shock Structure, University of Texas Report (1971).
10. J. B. McBride, M. Lampe, W. M. Manheimer, J. H. Orens, R. N. Sudan, and R. Shanny, Plasma Heating due to the Beam Cyclotron Instability, NRL Memorandum Report 2216 (February 1971).
11. D. Forslund, R. Morse, C. Nielson, and J. Fu, Phys. Fluids 15, 1303 (1972).
12. R. L. Briggs, Electron-Stream Interaction with Plasmas, (M. I. T. Press, Cambridge, Massachusetts 1964), p. 83.
13. M. S. Kovner, Soviet Phys. JETP, 13, 369 (1961).
14. A. R. Kantrowitz and H. E. Petschek, MHD Characteristics and Shock Waves in Plasma Physics in Theory and Application, (W. B. Kunchel, ed., New York, McGraw, 1966) pp. 148-206.
15. R. M. Patrick and E. R. Pugh, Phys. Fluids, 12, 366 (1969).